

Geometry and Topology Tango in Ordered and Amorphous Chiral Matter

M. Guzmán^{*}, D. Bartolo, D. Carpentier

ENS de Lyon, CNRS, Laboratoire de Physique, Lyon, France

^{*} marcelo.guzman-jara@ens-lyon.fr

June 17, 2021

1 Abstract

2 Systems as diverse as mechanical structures and photonic metamaterials enjoy
3 a common geometrical feature: a sublattice or chiral symmetry first introduced
4 to characterize electronic insulators. We show how a real-space observable, the
5 chiral polarization, distinguishes chiral insulators from one another and resolve
6 long-standing ambiguities in the very concept of their bulk-boundary corre-
7 spondence. We use it to lay out generic geometrical rules to engineer topo-
8 logically distinct phases, and design zero-energy topological boundary modes
9 in both crystalline and amorphous metamaterials.

10

11 Contents

12	1 Introduction	1
13	2 From chiral charge to chiral polarization and Zak phases	2
14	2.1 Chiral charge and chiral polarization.	2
15	2.2 Chiral polarization: an interplay between Zak phases and frame geometry.	4
16	3 Topology of chiral insulators	5
17	3.1 Sublattice Zak phases and winding numbers.	5
18	3.2 Disentangling Hamiltonian topology from frame geometry.	7
19	3.3 Inferring band topology from frame geometry.	9
20	3.4 Chiral polarization in the presence of a net chiral charge.	9
21	4 Bulk-boundary correspondence	9
22	5 Amorphous Chiral Insulators	10
23	5.1 Topological zero modes on amorphous chiral frames.	12
24	5.2 Topological zero modes of disordered chiral Hamiltonians.	13
25	5.3 Designing topologically protected zero modes in amorphous chiral matter.	14
26	5.4 Measuring the chiral polarization.	15
27	6 Conclusion	16
28	A Bloch theory convention and Wannier states.	17
29	A.1 Conventions for the Bloch decomposition.	17
30	A.2 Wannier functions.	17
31	A.3 Projected position operator and sublattice Zak phases.	18

32	B Chiral polarization, Zak phases and winding.	18
33	B.1 Chiral polarization and sublattice Zak phases.	18
34	B.2 Chiral polarization in different Bloch conventions.	19
35	B.3 Quantization of the intercellular Zak-phase in chiral insulators.	19
36	B.4 Relating the sublattice Zak phases to the winding of the Bloch Hamiltonian.	21
37	B.5 Quantization of the sublattice Zak phases.	21
38	B.6 How does the winding number of a chiral Bloch Hamiltonian change upon	
39	unit cell redefinition?	21
40	C Zero energy flat-band insulators.	22
41	D Chiral polarization in amorphous materials.	24
42	E Chiral polarization of time evolved Wannier states.	25
43	References	26

44

45

46 1 Introduction

47 A century after the foundations of band theory in solids by Félix Bloch [1], physicists have
 48 discovered new states of electronic matter ranging from insulators to superconductors by
 49 exploiting the topological structure of Bloch theory [2–7]. This topological revolution
 50 has built on two cornerstones: an abstract classification based on symmetries [8–15], and
 51 the practical correspondence between bulk topology and the boundary states measurable
 52 in experiments [2–6, 16–19]. During the past decade, these two generic principles spread
 53 frantically across fields as diverse as photonics, acoustics, or mechanics, leading to design
 54 principles and practical realizations of maximally robust waveguides [20, 21].

55 Among the number of symmetries constraining wave topology, chiral symmetry has
 56 a special status. Out of the three fundamental symmetries of the overarching ten-fold
 57 classification [8–10], it is the only one naturally realized with both quantum and classical
 58 waves. It generically takes the form of a sub-lattice symmetry when waves propagate
 59 in frames composed of two connected lattices A and B , with couplings only between, A
 60 and B sites, see e.g. Fig. 1a. In electronic systems, the archetypal example of a chiral
 61 insulator is provided by the polyacetylene molecule described by the Su-Schrieffer-Hegger
 62 (SSH) model [22]. In mechanics, the Hamiltonian description of bead-and-spring networks
 63 is intrinsically chiral [23–26]: the A sites correspond to the beads, and the B sites to
 64 the springs. In topological photonics and cold atoms chiral wave guides are among the
 65 simplest realizations of topological phases. Over the past decade, the modern theory
 66 of electronic polarization based on Zak phases and non-Abelian Wilson loops [27–30] has
 67 illuminated the intimate relation between crystalline symmetries and the topology of band
 68 structures [11–15]. By contrast, the role of chiral symmetry has been overlooked.

69 In this article, by introducing the concept of chiral polarization we determine the zero-
 70 mode content of interfaces between topologically incompatible crystalline and amorphous
 71 chiral meta(materials)

72 In the bulk, the chiral charge, which measures the imbalance between the number
 73 of sites on the sub-frames A and B , predicts the number of zero-energy modes of all
 74 Hamiltonians defined on a given chiral frame. To characterize chiral insulators we define

75 their chiral polarization $\mathbf{\Pi}$ as the spatial imbalance of the bulk waves on the two sub-
 76 frames. This material property does not rely on any crystalline symmetry and can therefore
 77 be defined locally on disordered and amorphous frames. In crystals, although akin to the
 78 time-reversal polarization of \mathbb{Z}_2 insulators [31], we show that $\mathbf{\Pi}$ is not merely set by the
 79 Bloch-Hamiltonian topology but also by the underlying frame geometry. At boundaries,
 80 we show how $\mathbf{\Pi}$ prescribes the surface chiral charge, and therefore the full zero-energy
 81 edge content of crystalline and amorphous chiral matter. Finally, we propose a series of
 82 practical protocols to experimentally measure the chiral polarization of mechanical, and
 83 photonic chiral metamaterials.

84 2 From chiral charge to chiral polarization and Zak phases

85 Introducing the concepts of chiral charge and polarization, we demonstrate that bulk prop-
 86 erties of chiral matter are determined by an intimate interplay between the frame topology,
 87 the frame geometry and the chiral Zak phases of Bloch Hamiltonians.

89 2.1 Chiral charge and chiral polarization.

90 We consider the propagation of waves in chiral material associated to d -dimensional frames
 91 including two sub-frames A and B . The wave dynamics is defined by a Hamiltonian \mathcal{H} .
 92 By definition, the chiral symmetry translates in the anti-commutation of \mathcal{H} with the chiral
 93 unitary operator $\mathbb{C} = \mathbb{P}^A - \mathbb{P}^B$, where \mathbb{P}^A and \mathbb{P}^B are the two orthogonal projectors on
 94 the sub-frames A and B . Simply put, in the chiral basis where \mathbb{C} is diagonal, \mathcal{H} is block
 95 off-diagonal.

96 In order to determine the relative weight of the wave functions of \mathcal{H} on the two sub-
 97 frames, we introduce the chiral charge

$$\mathcal{M} = \langle \mathbb{C} \rangle, \quad (1)$$

98 where the average is taken over the complete Hilbert space. Using the basis of fully
 99 localized states, we readily find that \mathcal{M} is fully prescribed by the frame topology: the chiral
 100 charge counts the imbalance between the number of A and B sites: $\mathcal{M} = N^A - N^B$. We
 101 can however also evaluate Eq. (1) in the eigenbasis of \mathcal{H} . Indexing by n the eigenenergies
 102 of \mathcal{H} , the eigenstates of the chiral Hamiltonian come by pairs of opposite energies related
 103 by $|-n\rangle = \mathbb{C}|n\rangle$. Chirality therefore implies that the chiral charge is solely determined
 104 by the zero modes of \mathcal{H} as $\mathcal{M} = \sum_n \langle n | \mathbb{C} | n \rangle = \langle 0 | \mathbb{C} | 0 \rangle$. Noting that the $|0\rangle$ states are
 105 eigenstates of the chiral operator with eigenvalue $+1$ when localized on the A sites and
 106 -1 when localized on the B sites, it follows that \mathcal{M} also is an algebraic count the zero
 107 modes of \mathcal{H} :

$$\mathcal{M} = N^A - N^B = \nu^A - \nu^B. \quad (2)$$

108 This equality is the classical result established by Maxwell and Calladine in the context of
 109 structural mechanics [33, 34] and independently discussed by Sutherland in the context of
 110 electron localization [35]. Eq. (2) implies that the spectral properties of \mathcal{H} are constrained
 111 by the frame topology. In particular, frames with a non-vanishing chiral charge impose
 112 *all* chiral Hamiltonian to possess flat bands. This simple prediction is illustrated in Fig. 1
 113 where we show the Lieb and the dice lattices, which are both characterized by a unit
 114 chiral charge per unit cell. All Hamiltonians defined on these lattices are therefore bound
 115 to support at least one flat band, Fig. 1b. No chiral insulators exist on the Lieb and dice
 116 lattices.

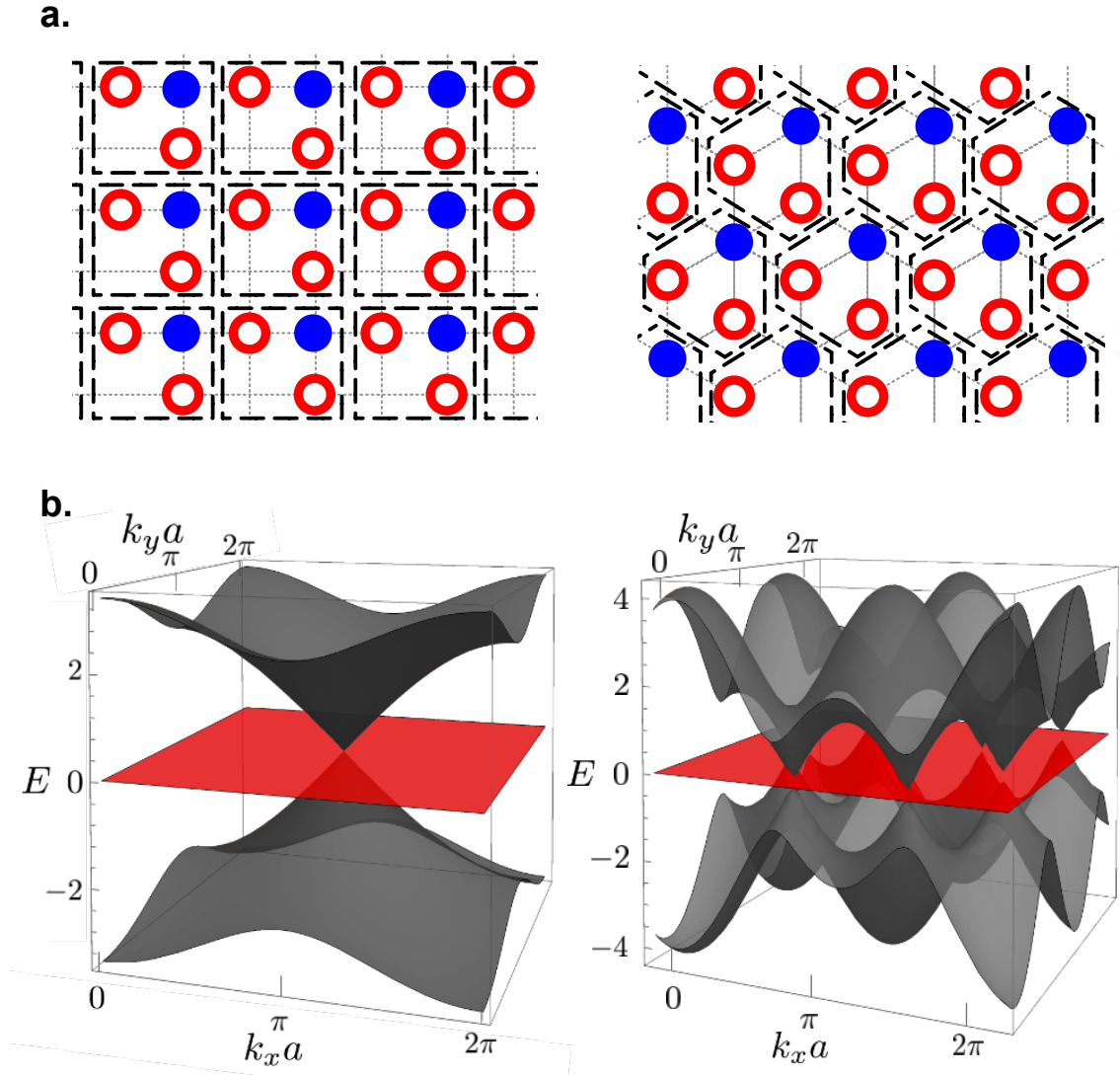


Figure 1: **Lattices with a finite chiral charge.** **a.** The Lieb (left) and dice (right) frames are both characterized by an imbalance between the number N^A and N^B of sites. In both cases the chiral charge per unit cell equals 1. Any Hamiltonian defined on these frames possesses a flat energy band. **b.** Illustration of two band spectra associated to chiral Hamiltonians defined on the Lieb (left) and dice (right) frames. The two band spectra are computed for tight-binding Hamiltonians with nearest neighbour coupling and a hopping parameter set to 1, see e.g. [32].

117 By contrast, in chiral insulators, no zero-energy bulk modes exist and \mathcal{M} must vanish.
 118 To probe the relative weight of the wave functions on the two sub-frames, we therefore
 119 introduce the chiral polarization vector $\Pi_j = \langle \mathbb{C}x_j \rangle_{E \neq 0}$. As the $|\pm n\rangle$ states contribute
 120 equally to Π in chiral systems, we henceforth use the definition

$$\Pi_j = 2 \langle \mathbb{C}x_j \rangle_{E < 0}, \quad (3)$$

121 with $j = 1, \dots, d$ are the indices of the d crystallographic directions and where $E < 0$
 122 indicates that the average is taken over the occupied states. Although seemingly identical
 123 to the the skew polarization introduced in [36, 37] for topological insulators, and the
 124 mean chiral displacement of quantum walks [38], we emphasize that Π_j does not rely on

125 any Bloch representation and is therefore defined also in amorphous phases. We stress
 126 that, even in the crystalline case, Π_j includes content beyond the skew polarization, as it
 127 resolves the weighted positions with a sub-unit-cell resolution. These differences are not
 128 mere technicalities, and will prove crucial in the next sections.

129 To gain more physical insight, it may be worth noting that in electronic systems, Π_j
 130 corresponds to the algebraic distance between the charge centers associated to the A and
 131 B atoms. While in mechanical networks, Π_j is the vector connecting the stress-weighted
 132 and displacement-weighted positions. A vanishing polarization indicates that the average
 133 locations of the stress and displacement coincide. Conversely, a finite chiral polarization
 134 reveals an asymmetric mechanical response discussed in [39, 40]. For the sake of clarity,
 135 before revealing topologically protected zero modes in amorphous phases, we first explore
 136 the consequences of a finite chiral polarization in periodic systems such as in the paradigm-
 137 atic example of the SSH model illustrated Fig. 2.

138

139 2.2 Chiral polarization: an interplay between Zak phases and frame 140 geometry.

141 We begin with a thorough discussion of crystalline materials, defined by periodic frames
 142 and Bloch Hamiltonians. Building on previous works on the electronic polarization [27–
 143 30],

144 we relate the chiral polarization of a crystalline material to the two Zak phases of waves
 145 projected on sub-lattices A and B when transported across the Brillouin zone. To do so, we
 146 first choose a unit cell and consider the basis of Bloch states $|\mathbf{k}, \alpha\rangle = \sum_{\mathbf{R}} e^{i\mathbf{k}\cdot\mathbf{R}} |\mathbf{R} + \mathbf{r}_\alpha\rangle$,
 147 where \mathbf{R} is a Bravais lattice vector, α labels the atoms in the unit cell and \mathbf{k} is the
 148 momentum in the Brillouin Zone (BZ). We henceforth use a convention where the Bloch
 149 Hamiltonian $H(\mathbf{k})$ is periodic in the BZ, see [28, 41] and Methods. More quantitatively,
 150 considering first Hamiltonians with no band crossing ¹, we define the A sub-lattice Zak
 151 phase of the n^{th} energy band along the crystallographic direction j as

$$\gamma_j^A(n) = i \int_{\mathcal{C}_j} d\mathbf{k} \langle u_n | \mathbb{P}^A \partial_{\mathbf{k}} \mathbb{P}^A | u_n \rangle, \quad (4)$$

152 where the $|u_n(\mathbf{k})\rangle$ are the eigenstates of $H(\mathbf{k})$, and \mathcal{C}_j the non-contractible loops over the
 153 Brillouin zone defined along the d crystallographic axes. $\gamma_j^B(n)$ is defined analogously
 154 on the B sublattice. The (intercellular) Zak phase is given by the sum of $\gamma_j^A(n)$ and
 155 $\gamma_j^B(n)$ [43]. In Methods, we show how to decompose the chiral polarization into a spectral
 156 and a frame contribution:

$$\Pi_j = \frac{a}{\pi} (\gamma_j^A - \gamma_j^B) + p_j, \quad (5)$$

157 where a is the lattice spacing (assumed identical in all directions), γ_j^A and γ_j^B are the
 158 sublattice Zak phases defined by

$$\gamma_j^A = \sum_{n < 0} \gamma_j^A(n). \quad (6)$$

159 In Eq. (5) the p_j are the components of the geometrical-polarization vector connecting the
 160 centers of mass of the A and B sites in the unit-cell:

$$\mathbf{p} = \sum_{\alpha \in A} \mathbf{r}_\alpha - \sum_{\alpha \in B} \mathbf{r}_\alpha. \quad (7)$$

¹In the situation where bands cross, our results should be generalized resorting to the Wilson loops of the non-commutative Berry connexion instead of the abelian Zak phase connection [42].

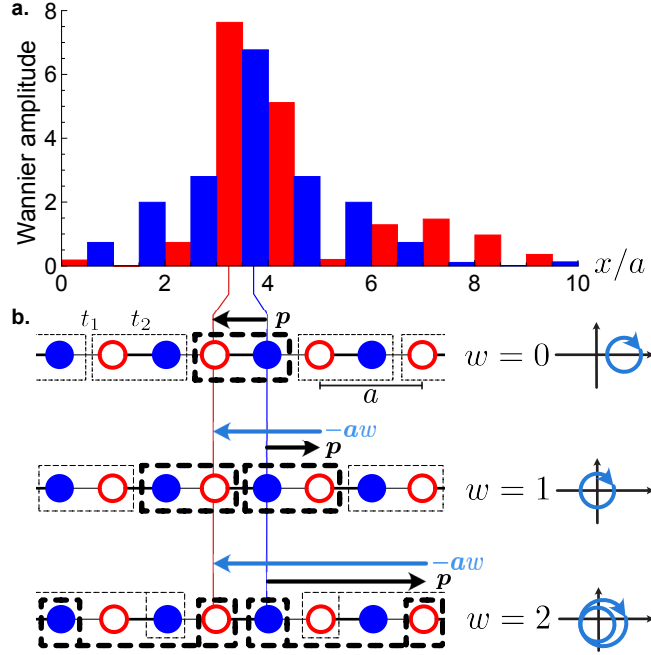


Figure 2: **Chiral polarization and Wannier functions.** **a.** Square of the Wannier amplitude projected into the A (red) and B (blue) sublattices for the ground state configuration of the two-band SSH model with hopping ratio $t_1/t_2 = 0.79$. a denotes the period of the 1D frame. The chiral polarization $\Pi = \langle x^A \rangle - \langle x^B \rangle$ is negative: the chain is left polarized regardless of the choice of unit cell. **b.** The winding number of the Bloch Hamiltonian encodes the chiral polarization *relative* to a given unit cell. The chiral polarization being a material property, the winding number w can therefore take any integer value when redefining the geometry of the unit cell as illustrated in the last column. Whatever the choice of the unit cell, the difference between the geometrical polarization and aw has a constant value given by the chiral polarization Π .

161 In crystals, Eqs. 5 quantifies the difference between the polarity of the ground-state wave
 162 function Π and the geometric polarization of the frame p . This difference is finite only
 163 when the two sublattice Zak phases differ.

164 3 Topology of chiral insulators

165 We now elucidate the intimate relation between the chiral polarization and the band topol-
 166 ogy of chiral gapped phases defined on periodic lattices. We outline the demonstrations
 167 of our central results below and detail them in Methods.

168

169 3.1 Sublattice Zak phases and winding numbers.

170 Computing the Wilson loop of the non-Abelian connection $\mathbf{A}_{n,m}(\mathbf{k}) = \langle u_n(\mathbf{k}) | \partial_{\mathbf{k}} | u_m(\mathbf{k}) \rangle$
 171 along \mathcal{C}_j , we show that chirality relates the d Zak phases $\gamma_j^A + \gamma_j^B$ to the windings of the
 172 Bloch Hamiltonian as

$$\gamma_j^A + \gamma_j^B = \pi w_j + 2\pi\mathbb{Z}, \quad (8)$$

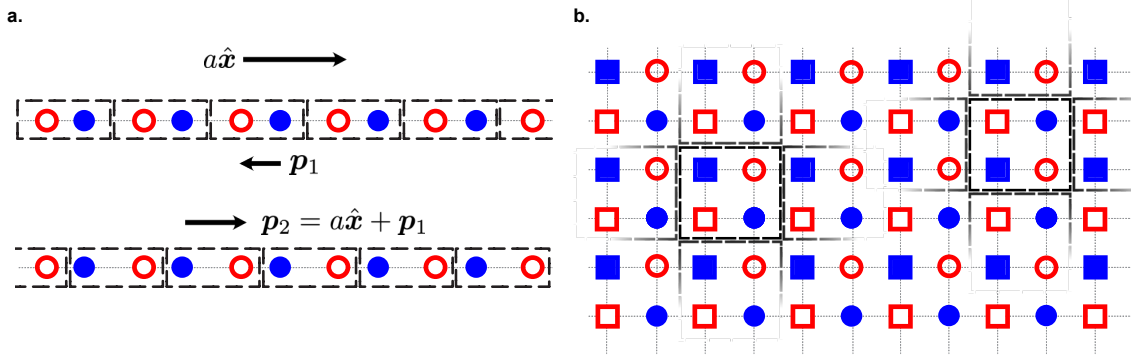


Figure 3: **Inferring the band topology from frame geometry.** **a.** The two-sites Wigner-Seitz cell on a 1D chiral frame have different geometrical polarizations; their difference is given by one Bravais vector. Consequently, we can always define the unit cell so that the Bloch Hamiltonian has a finite winding. **b.** All the Wigner-Seitz unit cells on the checkerboard lattice share the same (vanishing) chiral polarization. Therefore a single winding number w characterizes the Hamiltonians on this frame in virtue of Eq. (11). Evaluating the winding using the Wigner-Seitz cell compatible with the atomic limit of \mathcal{H} yields $w = 0$, by definition.

173 where $w_j = i/(4\pi) \int_{\mathcal{C}_j} d\mathbf{k} \cdot \text{Tr}[\partial_{\mathbf{k}} H C H^{-1}] \in \mathbb{Z}$. The total Zak phase is quantized but the
 174 arbitrary choice of the origin of space implies that both γ^A and γ^B are only defined up
 175 to an integer. As a matter of fact, a mere $U(1)$ gauge transformation $|u_n\rangle \rightarrow e^{i\alpha_n(k)} |u_n\rangle$
 176 arbitrarily modifies $\gamma_j^A(n)$ and $\gamma_j^B(n)$ by the same quantized value: $\gamma_j^A(n) \rightarrow \gamma_j^A(n) +$
 177 πm , $\gamma_j^B(n) \rightarrow \gamma_j^B(n) + \pi m$, with $m \in \mathbb{Z}$. By contrast, the difference between the two
 178 sublattice Zak phases is left unchanged by the same gauge transformation which echoes
 179 its independence from the space origin. Evaluating the winding of $H(\mathbf{k})$ using the Bloch
 180 eigenstates (see Methods), we readily establish the essential relation²

$$\gamma_j^B - \gamma_j^A = \pi w_j \in \pi\mathbb{Z}. \quad (9)$$

181 Chirality quantizes the sublattice Zak phases of chiral insulators, even in the absence of
 182 inversion or any other specific crystal symmetry. γ_j^A and γ_j^B are however not independent.
 183 Combining Eqs. (8) and (9) we can always define the origin of space so that $\gamma_j^A = 0$ and
 184 $\gamma_j^B = \pi w_j$.

185 The d winding numbers of Eq. (9) characterize the topology of $H(\mathbf{k})$. In particular,
 186 if for a given Wigner-Seitz cell the corresponding $H(\mathbf{k})$ is associated to a finite winding
 187 ($w_j \neq 0$), then it cannot be smoothly deformed into the atomic limit defined over the
 188 same unit cell. The set of winding numbers is however poorly informative about the spa-
 189 tial distribution of the charges in electronic systems, or about the stress and displacement
 190 distributions in mechanical structures. The values of w_j are defined only up to the arbi-
 191 trary choice of unit cell required to construct the Bloch theory. A well known example
 192 of this limitation is given by the SSH model, where the winding of $H_{\mathbf{k}}$ can either take
 193 the values 0 or ± 1 depending on whether the unit cell's leftmost site belongs to the A
 194 or B sublattice, see Fig. 2a and Methods. We show in the next section, how the chiral
 195 polarization alleviates this limitation.

196

²Note that this difference of Zak phases was recently denoted as a chiral phase index in [45].

197 3.2 Disentangling Hamiltonian topology from frame geometry.

198 Equations (5) and (9) provide a clear geometrical interpretation of the winding number
199 w_j as the quantized difference between the geometrical and the chiral polarization:

$$\Pi_j = (p_j - a_j w_j). \quad (10)$$

200 We can now use this relation to illuminate the very definition of a chiral topological
201 insulator. The chiral polarization $\Pi_j = 2\langle \mathbb{C}x_j \rangle_{E<0}$ is a physical quantity that does not
202 depend on the specifics of the Bloch representation. Therefore computing Π_j for two unit
203 cells (1) and (2), we find that the windings of the two corresponding Bloch Hamiltonians
204 $H^{(1)}(\mathbf{k})$ and $H^{(2)}(\mathbf{k})$ are related via Eq. (10) as

$$w_j^{(2)} - w_j^{(1)} = \frac{1}{a_j} (p_j^{(2)} - p_j^{(1)}). \quad (11)$$

205 This essential relation implies that one can always construct a Bloch representation of \mathcal{H}
206 where $H(\mathbf{k})$ is topologically trivial, at the expense of a suitable choice of a unit cell. As
207 a matter of fact, a redefinition of the unit cell can increase, or reduce the geometrical
208 polarization, and therefore the winding numbers, by an arbitrary large multiple of a_j as
209 illustrated in Fig. 2b.

210 For instance in the case of Hamiltonians with nearest neighbor couplings, applying
211 Eq. (11) to Wigner Seitz unit cells ($|w_j| \leq 1$), we find that there exist as many topological
212 classes of \mathcal{H} , as different geometrical polarizations in the Wigner-Seitz cells. This number
213 provides a direct count of the chiral 'atomic limits' of \mathcal{H} .

214 Defining the topology of a chiral material therefore requires characterizing both the
215 winding of its Bloch Hamiltonian, and the frame geometry. Remarkably, this interplay
216 provides an insight on topological band properties from the sole inspection of the frame
217 structure.

218

219 3.3 Inferring band topology from frame geometry.

220 There exists no trivial chiral phase in one dimension: one can always choose a Wigner-Seitz
221 cell such that the Bloch representation of \mathcal{H} has a non-vanishing winding. As a matter of
222 fact, the geometrical polarization of the Wigner-Seitz cells can only take two finite values
223 of opposite sign depending on whether the leftmost site in a unit cell is of the A or B type,
224 see Fig. 3a. Equation (11) therefore implies that, in $1D$, there always exists, at least, two
225 topologically distinct gapped phases smoothly connected to two atomic limits. The two
226 gapped phases are characterized by two distinct pairs of winding numbers defined by two
227 inequivalent choices of unit cells. In other words all SSH Hamiltonians are topological.

228 Similarly, in $d > 1$ only frames having a geometrical polarization invariant upon re-
229 definition of the Wigner-Seitz cell can support topologically trivial Hamiltonians. Equa-
230 tion (11) indeed implies that a topologically trivial Hamiltonian \mathcal{H} constrains the frame
231 geometry to obey $p_j^{(1)} = p_j^{(2)}$ for all pairs of unit cells and in all directions j . We show a
232 concrete example of such a frame in Fig. 3b.

233 Before discussing the crucial role of the frame topology and geometry on the bulk-
234 boundary correspondence of chiral phases, we extend these two notions to chiral insulators
235 with a flat band.

236

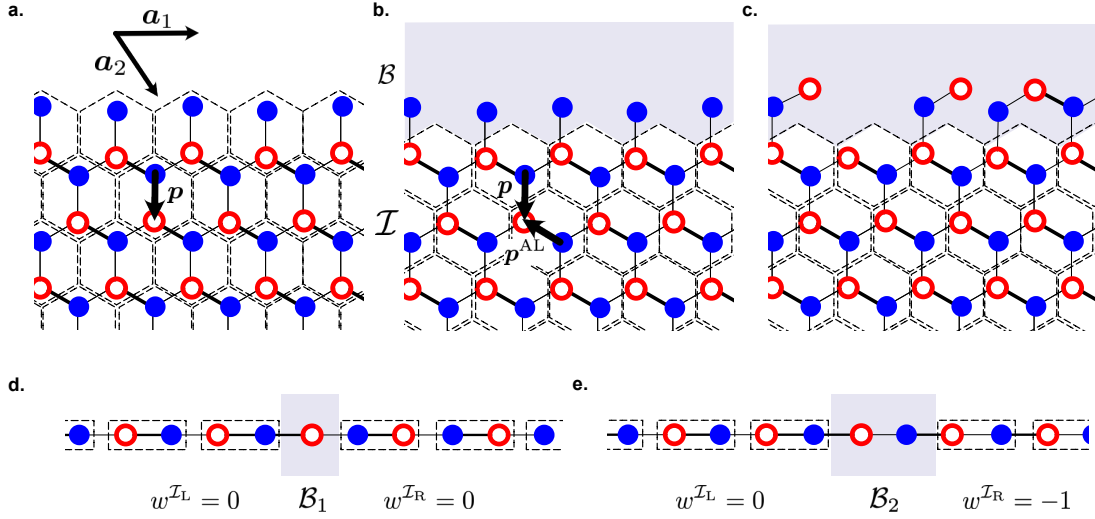


Figure 4: **Bulk-boundary correspondence.** **a.** A chiral crystal defined on a honeycomb frame is terminated by a clean zigzag edge incompatible with the atomic-limit Hamiltonian defined by keeping only the dominant couplings represented by thick solid lines. The dashed rectangles indicate the Wigner-Seitz cells allowing a tessellation compatible with the edge geometry. The arrow indicates the geometrical polarization \mathbf{p} . **b.** Same physical system. The crystalline bulk is now tiled using the unit cell compatible with the atomic limit. This requires a redefinition of the crystal boundary \mathcal{B} (shaded region). The arrows indicate the geometrical polarization of the new unit cell (\mathbf{p}^{AL}). The difference $\mathbf{p} - \mathbf{p}^{AL}$ is a Bravais lattice vector (\mathbf{a}_2). **c.** Same material as in (a.) and (b.) including a disordered interface \mathcal{B} bearing a non-zero chiral charge $\mathcal{M}^{\mathcal{B}}$. **d.** Two connected SSH chains. The Wigner-Seitz cell in the two materials are compatible with their atomic limits. The interface \mathcal{B}_1 separating the two materials is one-site wide. **e.** Redefining the Wigner-Seitz cell on the right hand side of the interface requires widening the boundary region. This redefinition makes the unit cell incompatible with the atomic limit. The winding of the Bloch Hamiltonian in \mathcal{I}_R takes a finite value and consequently modifies the zero-mode content of the boundary region.

237 3.4 Chiral polarization in the presence of a net chiral charge.

238 It is worth noting that the chiral polarization can also be defined and computed in the
 239 presence of an additional zero-energy flat band in the gap. As detailed in the Methods
 240 section, it then takes the form

$$\Pi_j = (p_j - p_j^{\text{ZM}}) + a (\gamma_j^A - \gamma_j^B) / \pi. \quad (12)$$

241 In this case, we lose the clear decomposition Π into geometrical and topological con-
 242 tributions. The geometrical polarization is corrected by p^{ZM} which originates from a
 243 spectral contribution associated to the zero-energy band. Furthermore the second term
 244 on the r.h.s., the difference between two geometrical Zak phases, is not a topological wind-
 245 ing number anymore. Despite the seemingly complex form of Eq. (12), we show in the
 246 next section that the chiral polarization remains an effective tool to relate spectral bulk
 247 properties to the number of zero-energy states localized at boundaries.

248 4 Bulk-boundary correspondence

249 We now establish a bulk-boundary correspondence relating the chiral polarization to the
 250 number of zero modes supported by the free surface of a chiral insulator. For the sake of
 251 clarity, we discuss the two-dimensional case without loss of generality. We consider first a
 252 crystalline insulator \mathcal{I} terminated by a clean edge $\partial\mathcal{I}$ oriented along a Bravais vector, say
 253 \mathbf{a}_1 as illustrated in Fig. 4a.

254 The bulk of the insulator can be described by different types of unit cells. As illustrated
 255 in Fig. 4a, in the presence of a clean edge, it is natural to choose a unit cell which allows
 256 a tessellation of the whole system. However, this unit cell is generically incompatible with
 257 the atomic limit of the Hamiltonian, and therefore does not allow a direct count of the zero
 258 energy boundary states using the simple Maxwell-Calladine count. An obvious strategy
 259 hence consist in redefining the unit cell, as in Fig. 4b to match the constraints of the
 260 atomic limit. This redefinition comes at the expense of leaving sites outside of the bulk
 261 tessellation. We define this ensemble of sites as the boundary region \mathcal{B} . Keeping in mind
 262 that we can smoothly deform the Hamiltonian into its atomic limit without closing the
 263 gap, we use Eq. (2) to count the number of zero energy states hosted by \mathcal{B} . It is given by
 264 $\mathcal{V} = \mathcal{M}^{\mathcal{B}}$. An essential geometrical observation is that the net chiral charge in \mathcal{B} can be
 265 expressed as $\mathcal{N}^{\partial\mathcal{I}}(p_2^{\text{AL}} - p_2)$, where $\mathcal{N}^{\partial\mathcal{I}}$ is the edge length expressed in number of unit cells
 266 and p_2 is the geometrical polarization of the initial unit cell. We can now make use of the
 267 invariance of the chiral polarization formalized by Eq. (11) to relate the geometrical count
 268 of zeromodes to the winding of the Bloch Hamiltonian: $\mathcal{V} = \mathcal{N}^{\partial\mathcal{I}}(p_2^{\text{AL}} - p_2) = \mathcal{N}^{\partial\mathcal{I}} w_2^{\mathcal{I}}$. To
 269 arrive at a bulk boundary correspondence generic to all chiral insulators, we include the
 270 possibility of dealing with irregular interfaces featuring a net chiral charge $\mathcal{M}^{\mathcal{B}}$ as sketched
 271 in Fig. 4c. We then find

$$\mathcal{V} = \mathcal{M}^{\mathcal{B}} + \mathcal{N}^{\partial\mathcal{I}} w_2^{\mathcal{I}}. \quad (13)$$

272 Three comments are in order. Firstly, the bulk boundary correspondence defined by
 273 Eq. (13) illuminates the geometrical implication of a nonzero winding: a finite $w_2^{\mathcal{I}}$ echoes
 274 the impossibility to tile a periodic frame with unit cells γ compatible with the Hamiltonian's
 275 atomic limit. Secondly, Eq. (13) is readily generalized to interfaces separating two chiral
 276 insulators \mathcal{I}_L and \mathcal{I}_R , where we simply have to apply the same reasoning on each side of
 277 the interface: $\mathcal{V} = \mathcal{M}^{\mathcal{B}} + \mathcal{N}^{\partial\mathcal{I}}(w_2^{\mathcal{I}_L} + w_2^{\mathcal{I}_R})$, see e.g. Figs. 4d and 4e. Thirdly, the formula
 278 given by Eq. (13) generalizes the Kane-Lubensky index introduced in their seminal work to
 279 count the zero-energy modes localized within isostatic mechanical networks [25]. We show

280 that this index defines a bulk-boundary correspondence generic to all chiral insulators
 281 and even to flat band insulators such as hyperstatic lattices as further discussed in the
 282 Methods section.

283 5 Amorphous Chiral Insulators

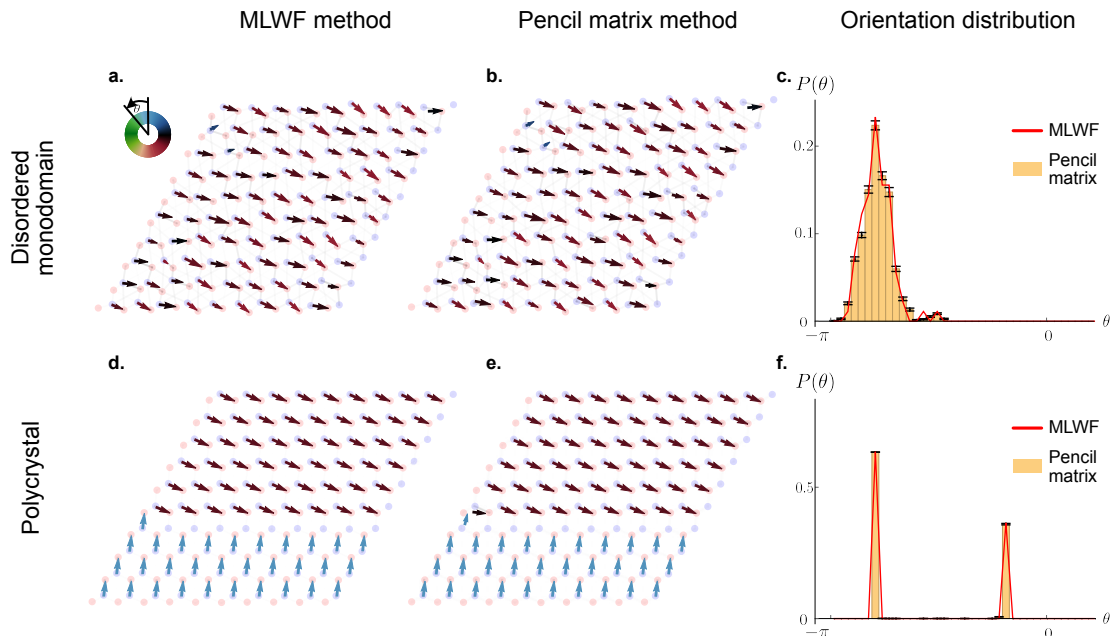


Figure 5: **Pencil matrix versus maximally localized Wannier functions** **a.** Single domain configuration with geometrical and spectral disorder. The chiral polarization field obtained from the maximally localized wannier functions is superposed. **b.** Chiral polarization field obtained from one realization of the pencil matrix procedure. **c.** Orientation distribution obtained from 50 values of α (bar chart), and from the maximally localized wannier functions (red solid line). **d.**, **e.**, **f.** correspond to the same information, this time for two crystalline domains.

284 In condensed matter, chiral symmetry is a low energy feature of electronic Hamilto-
 285 nians, which is unlikely to survive to strong structural disorder. Conversely, in photonic,
 286 acoustic or mechanical metamaterials chirality is built in by design and can therefore be
 287 present both in ordered or amorphous structures [20, 46]. In mechanical metamaterials
 288 chirality is even more robust as it is inherent to any system assembled from elastically
 289 coupled degrees of freedoms [21]. In this section, we show how to generalize our physical
 290 characterization of zero energy modes to disordered chiral metamaterials.

291 Over the past two years a number of experimental, numerical and theoretical works
 292 showed that crystalline symmetries are not required to define topological insulators, see
 293 e.g. [47–50]. Unlike these pioneering studies where topologically inequivalent disordered
 294 phases are distinguished by abstract indices defined in real space and related to the quan-
 295 tification of edge currents, our framework solely based on the chiral polarization applies
 296 to chiral systems regardless of the presence or not of time reversal symmetry.

297 Our strategy follows from the fundamental relation: $\Pi_j = p_j - a_j w_j$ of Eq. (10). This

298 relation implies a one-to-one correspondence between the chiral polarization and a topo-
 299 logical spectral property quantized by the winding vector. The basic idea hence consists
 300 in probing the existence of topologically protected zero modes by *local* discontinuities in
 301 the chiral polarization field, even when no winding number or Zak phase can be defined.
 302 Relating topologically protected excitations to real-space singularities requires defining a
 303 local chiral polarization field $\mathbf{\Pi}(\mathbf{x})$. By definition, $\mathbf{\Pi}(\mathbf{x})$ measures the local imbalance of
 304 the wave function carried by the A and B sites. To express $\mathbf{\Pi}(\mathbf{x})$, it would be natural to
 305 consider eigenstates of the position operator $P\mathbf{x}P$ projected onto the occupied states of \mathcal{H} .
 306 However, in dimension $d > 1$, the different components of the projected position operator
 307 do not commute $[Px_jP, Px_kP] \neq 0$ for $j \neq k$, and do not possess common eigenstates.
 308 Instead, we express the polarisation in terms of the maximally localized states \widetilde{W}_m [28],
 309 which are centered on the position $\mathbf{x}_m \equiv \langle \widetilde{W}_m | \widehat{X} | \widetilde{W}_m \rangle$. These states generalize the Wan-
 310 nier functions in the absence of translational symmetry, see Methods for more details. We
 311 can then define the *local* chiral polarization as the weighted chiral position evaluated over
 312 \widetilde{W}_m :

$$\mathbf{\Pi}(\mathbf{x}_m) = 2 \langle \widetilde{W}_m | C\widehat{X} | \widetilde{W}_m \rangle. \quad (14)$$

313 In practice, we can bypass the time consuming numerical determination of the \widetilde{W}_m
 314 by taking advantage of the so-called pencil-matrix method [51]. In short, the method
 315 consists in replacing in (14) the \widetilde{W}_m by eigenstates of a linear combination of the projected
 316 position components $R = \sum_j \alpha_j Px_jP$; $\sum \alpha_j = 1$. The dependence on α_i of the resulting
 317 chiral polarization is a measure of the non-commutativity of the Px_j typically associated
 318 to a nonvanishing Berry curvature. In practice, as illustrated in Fig. 5, the difference
 319 between the actual polarization, computed from the \widetilde{W}_m , and its approximation based on
 320 the R -matrix eigenstates is smaller than the distance between neighboring sites. Given
 321 the excellent agreement found both in mono and polycrystals, we henceforth use the
 322 pencil matrix method to locally measure the chiral polarization fields in disordered and
 323 amorphous structures out of reach of conventional chiral displacement characterizations
 324 [52].

325 To make the discussion as clear as possible we consider separately the two possible
 326 sources of randomness in a disordered chiral insulator: (i) geometrical disorder, which
 327 affects the frame geometry leaving the interaction between the A and B sites unchanged
 328 and (ii) Spectral disorder, which alters the interactions while leaving the frame geometry
 329 unchanged.

330

331 5.1 Topological zero modes on amorphous chiral frames.

332 The reasoning is easily explained starting from a concrete example. Fig. 6 shows the
 333 interface between two topologically distinct insulators, \mathcal{I}_T and \mathcal{I}_B , living on a honeycomb
 334 frame. They correspond to distinct atomic limits of a nearest-neighbor tight binding
 335 Hamiltonians including two different hopping coefficients, see e.g. [53]. For the choice of
 336 unit cell sketched in Fig. 6, the winding vectors are $\mathbf{w}^{\mathcal{I}_T} = (0, 1)$ and $\mathbf{w}^{\mathcal{I}_B} = (1, 0)$. As
 337 a result the boundary region \mathcal{B} hosts one zero mode per unit cell located on the A sites.
 338 As expected from Eq. (10), on a homogeneous periodic frame, $\mathbf{\Pi}(\mathbf{x})$ takes two distinct
 339 values in the two regions, and is discontinuous across \mathcal{B} . Correspondingly, the distribution
 340 of the chiral polarization in the sample consists of two peaks centered on the two values
 341 associated to two topologically inequivalent phases, see Fig. 6 (left column).

342 We now disorder the frame by shifting all site positions by random displacements of
 343 maximal amplitude $|\delta\mathbf{x}|$ while preserving the magnitude of the interactions in the corre-

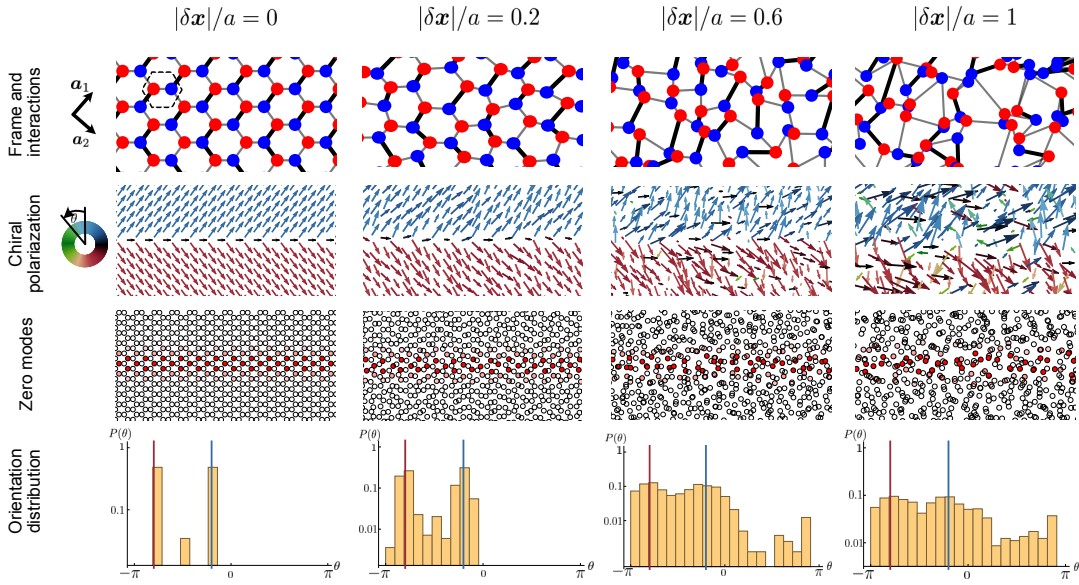


Figure 6: **Topological zero energy states on amorphous frames** First row: Sketch of the frame geometry for increasing positional disorder quantified by the maximal amplitude of the random displacements $|\delta\mathbf{x}|/a$. All panels show the vicinity of a boundary between two different insulators defined on the same frame but with different positions of the stronger couplings. The lines' width indicates the magnitude of the coupling strength. In all panels $t'/t = 20$. In the leftmost panel, we indicate the choice of the unit cell and of the crystallographic axes. Second row: Corresponding chiral polarization fields. The color indicates the orientation of $\mathbf{\Pi}(\mathbf{x})$ Third row: Magnitude of the zero-mode wave function. The zero mode is located at the boundary between topologically inequivalent states even on amorphous frames. Fourth row: Probability density function of the θ , the local orientation of the chiral polarization field. The distributions are peaked on the same two directions (vertical lines) regardless of the magnitude of disorder. This reveals the coexistence of two distinct topological phases robust to positional disorder.

344 sponding Hamiltonian \mathcal{H}_D . For sufficiently large displacements, it is impossible to keep
 345 track of the original periodic lattice, see Fig. 6 (first row). Nonetheless, we clearly see
 346 in the third row of Fig. 6 that the topologically protected zero modes located in \mathcal{B} are
 347 preserved, despite the lack of crystalline symmetry and the impossibility to define a Bloch
 348 Hamiltonian and its topological winding numbers. Note that unlike in [54] both the bulk
 349 and the boundary region are homogeneously disordered. Again, the existence and location
 350 of a line of zero modes is revealed by variations of the chiral polarization field. The vari-
 351 ations of the orientation of $\mathbf{\Pi}(\mathbf{x})$ occurs over the penetration length-scale ℓ_G set by the
 352 energy gap. The coexistence of two topologically distinct amorphous phases is signalled
 353 by a (wider) bimodal distribution of $\mathbf{\Pi}(\mathbf{x})$ peaked on the same values as in the pure case,
 354 see Fig. 6 (last row). This robust phenomenology is further illustrated in Supplementary
 355 Video 1, showing the evolution of the polarization field and zero-mode location as the
 356 magnitude of disorder is increased.

357 This observation reflects a generic feature of chiral matter. Randomizing the frame ge-
 358 ometry cannot alter the energy gap provided that the graph defined by the coupling terms
 359 of \mathcal{H} has a fixed chiral connectivity. This observation implies that the concept of topolog-
 360 ical phase naturally applies to amorphous frames that can be continuously deformed into

361 periodic lattices. In fact, the coexistence of different chiral insulators is effectively probed
 362 by the spatial distribution of the polarization field $\mathbf{\Pi}(\mathbf{x})$. Each peak of the distribution
 363 signals topologically inequivalent regions in amorphous chiral matter. The phase bound-
 364 aries are then readily detected by jumps of the chiral-polarization vector field over ℓ_G .
 365

366 5.2 Topological zero modes of disordered chiral Hamiltonians.

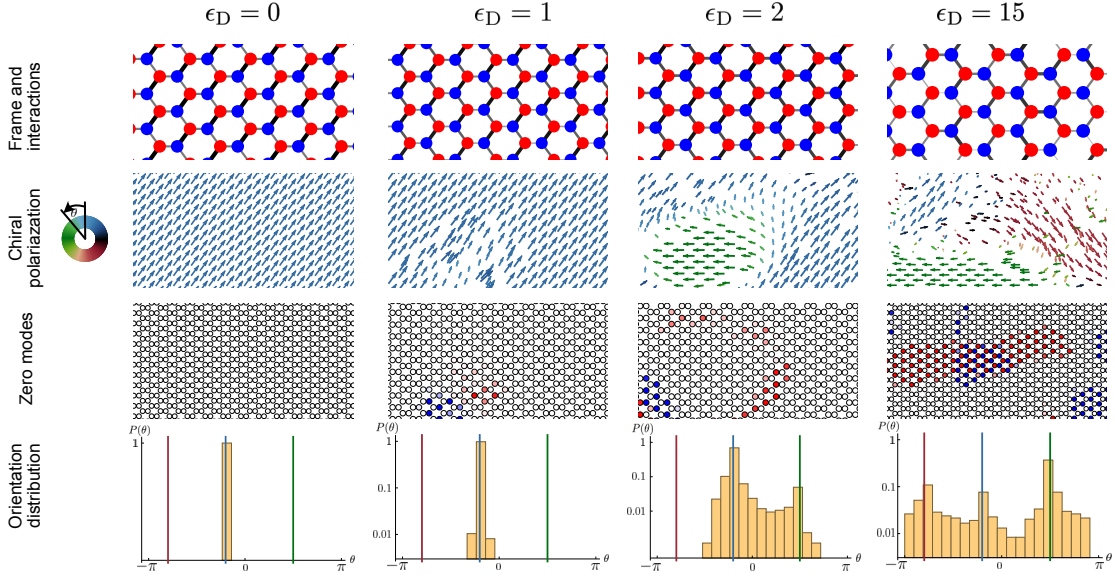


Figure 7: **Topological zero-energy states in the bulk of disordered chiral insulators** First row Sketch of the honeycomb frame and of the coupling strengths for increasing spectral disorder. The strengths of the couplings are represented by the width of the dark lines. Their randomness is quantified by the variance of the Gaussian couplings ϵ_D . The correlation length for all the examples is $\xi = 12a$. Second row Corresponding chiral polarization fields. The color indicates the orientation θ of $\mathbf{\Pi}(\mathbf{x})$. Third Row: Magnitude of the zero-energy modes on the A (red) and B (blue) sites. Fourth row: Probability density function of the orientation θ . Remarkably, even in the disordered cases, the distribution peaks only at values characteristic of the three phases of the homogeneous chiral Hamiltonian.

367 The case of spectral disorder is more subtle as it can trigger topological transitions.
 368 Again, we start with a concrete example. We use the same model of insulator as in the
 369 previous section. Considering the even simpler case of a perfect monocrystal, there is no
 370 zero mode in the sample. Keeping the frame unchanged we add disorder to the interactions
 371 in the form of random perturbations to the coupling parameters. We note ϵ_D the width
 372 of the Gaussian disorder distribution, ξ its correlation length and ΔE the energy gap in
 373 the pure case. When $\epsilon_D/\Delta E \ll 1$ no zero mode exists in this finite system see Fig. 7
 374 first column. Consistently, the local chiral polarization hardly fluctuates in space and its
 375 distribution remains peaked around the same constant value.

376 By contrast as $\epsilon_D/\Delta E \sim 1$, zero energy modes emerge in the bulk. Their presence
 377 signals local the emergence of topologically inequivalent regions in the material triggered
 378 by local gap inversions. The distinct phases are revealed by the orientational distribution of
 379 $\mathbf{\Pi}(\mathbf{x})$: as disorder increases additional peaks grow at values of θ characteristic of the other

380 two homogeneous topological insulators, Fig. 7 (last row). In the limit of strong disorder,
 381 the spatial extent of the coexisting phases is set by the disorder correlation length ξ as
 382 exemplified in Supplementary Movie 2. Gap closings also have a local signature in the
 383 polarization field. As $\mathbf{\Pi}(\mathbf{x}_m)$ is only defined at the generalized Wannier centers (Eq. (14)),
 384 $\mathbf{\Pi}(\mathbf{x}_m)$ cannot be computed at the center of a zero mode, which by definition does not
 385 support any Wannier mode. The proliferation of zero modes in the bulk is therefore
 386 signaled by an increasing number of holes in the polarization field.

387 The above observations do not rely on the specific model we use in Figs. 6 and 7.
 388 Generically, adding spectral disorder to a chiral Hamiltonian results in the nucleation of
 389 additional topological phases decorated by zero modes at their boundaries. Even in the
 390 absence of a Bloch theory, we can distinguish the topological nature of the coexisting
 391 phases by measuring their average chiral polarization. For spatially correlated disorder
 392 the spatial extent of each phase is set by the disorder correlation length ξ .

393

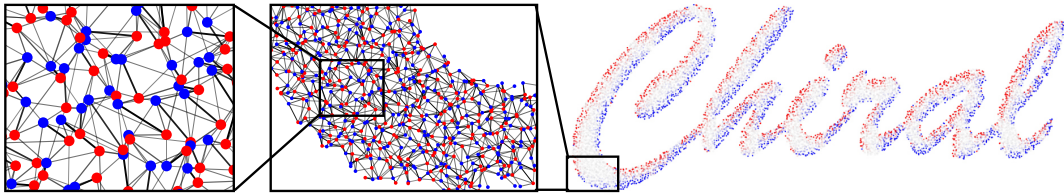


Figure 8: **Disordered chiral metamaterial** Macroscopic view and close ups on an amorphous frame supporting a disordered chiral insulator. The frame is defined adding a strong positional disorder to a Honeycomb lattice $|\delta\mathbf{x}| = a$. Using the same Hamiltonian as in Figs.6 and 7, we add spectral disorder corresponds to $\epsilon_D = 2$. Cutting the sample to form the word "chiral" reveals a continuous distribution of zero modes along the edge.

394 5.3 Designing topologically protected zero modes in amorphous chiral 395 matter.

396 It is worth stressing that disordered chiral insulators generically support topologically
 397 protected zero-energy modes at their boundaries. Unlike crystalline topological insulators,
 398 the lower the bulk and edge symmetries the more robust the edge states.

399 Cutting an amorphous sample into two parts without inducing the proliferation of
 400 boundary zero modes is virtually impossible. It would require cutting bonds while pre-
 401 serving the connectivity between all pairs of A and B site connected by the local polar-
 402 ization vectors $\mathbf{\Pi}(\mathbf{x}_m)$; only this type of configurations can be continuously deformed into
 403 crystals having edges matching that of tilings generated by the unit cell of an atomic limit.
 404 These cuts require extreme fine tuning in macroscopic samples and are therefore virtually
 405 impossible to achieve. This property makes the design of zero energy wave guides very
 406 robust in amorphous chiral matter. As illustrated in Fig. 8.

407

408 5.4 Measuring the chiral polarization.

409 In this section we show that the chiral polarization is not only a powerful theoretical
 410 concept, but an actual material property readily accessible to experiments. Two scenarios
 411 are possible: when the (low energy) eigenfunctions can be measured, the chiral polarization
 412 can be directly evaluated using its definition, Eq. (3). This technique is straightforward
 413 e.g. in mechanical metamaterials [55], where the vibrational eigenmodes can be imaged in
 414 real space in response to mechanical actuation.

415 Alternatively, when spectral properties are out of reach of quantitative measurements,
 416 we can infer the value of the chiral polarization from the dynamic spreading of localized
 417 chiral excitations. This approach builds and generalizes the technique pioneered in the
 418 context of periodically driven photonic quantum walk [56, 57]. For the sake of clarity we
 419 henceforth limit our discussion to 1D, two-band insulators although the reasoning applies
 420 in higher dimensions.

421 We introduce the dynamical chiral polarization $\Pi_\Psi(t) = \langle \Psi(t) | \mathbb{C}\hat{X} | \Psi(t) \rangle$ defined over
 422 the time-evolved states $\Psi(t) = \exp(-iHt)\Psi(0)$, where $\Psi(0)$ is a localized chiral state.
 423 Should one be able to initialize an experiment in a Wannier State $\Psi(0) = W_{n,\mathbf{R}}$, the wave
 424 function would spread as in Fig. 9a, but remarkably the dynamical chiral polarization
 425 $\Pi_\Psi(t)$ would be stationary and equal to Π in a homogeneous system as illustrated in
 426 Fig. 9a, and demonstrated in the Method section. In practice, it would be always eas-
 427 ier to approximate the Wannier state by excitations Ψ_{AB} (resp. Ψ_{BA}) localized on two
 428 neighboring A and B sites (resp. B and A). The result of this procedure is shown in
 429 Fig. 9b and reveals that the long-time dynamics of $\Pi_\Psi(t)$ converges towards the chiral
 430 polarization Π . However, we stress that the essential information about the orientation
 431 of Π is already accessible at very short times and would not suffer from possible damping
 432 issues. When $\Pi_\Psi(t=0)$ and Π have opposite signs, we observe very large amplitude oscil-
 433 lations reflecting the dynamic reversal of the chirality of the wave packet at short times.
 434 Conversely when $\Pi_\Psi(t=0)$ and Π are parallel the convergence is very fast and devoid of
 435 large amplitude fluctuations.

436 It is worth noting that the chiral initial state $\Psi(t=0) = \Psi_{AB}$ is an atomic-limit
 437 eigenstate. The dynamics can then be seen as the result of a quench at $t=0$ starting
 438 from the atomic-limit Hamiltonian. The amplitude of the fluctuations in Fig. 9b then
 439 reveals the topological nature of the quench. As a last comment we stress that although
 440 our protocol is close to the chiral displacement method introduced and used in [56–59], it
 441 is not tight to a Bloch Hamiltonian model, but characterizes an intrinsic (meta)material
 442 property.

443 6 Conclusion

444 We have established a generic framework to characterize, elucidate and design the topo-
 445 logical phases of chiral insulators. In crystals, we show that the frame topology and the
 446 frame geometry conspire with Bloch Hamiltonian topology to determine the zero-mode
 447 content of the bulk and interfaces. In the bulk, the frame topology fully determines the
 448 algebraic number of zero-energy modes counted by the chiral charge \mathcal{M} . Chiral insula-
 449 tors, however, are distinguished one another via their chiral polarization $\mathbf{\Pi}$ set both by
 450 the frame geometry and Bloch-Hamiltonian topology. At their surface, the number of
 451 zero-energy states is prescribed by the interplay between the Bloch Hamiltonian topology
 452 and the frame geometry in the bulk on one hand, and by the frame topology of the bound-
 453 ary on the other hand. This subtle tango goes beyond the bulk-boundary-correspondence
 454 principles solely based on Hamiltonian topology.

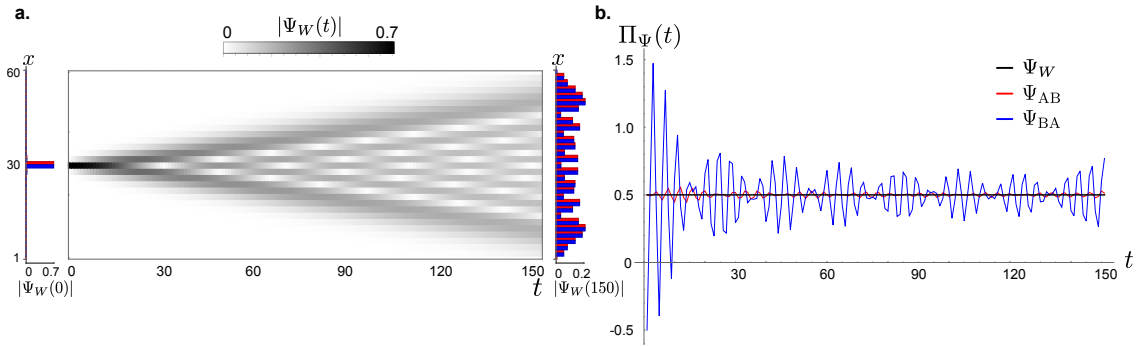


Figure 9: **Measuring the chiral polarization in time.** **a.** Left: Dynamical evolution of a Wannier state in the ground state of a two-band SSH model, with hopping ratio $t_1/t_2 = 0.1$. The state is localized in the middle of a finite system of 60 unit cells. Center: Time evolution of the wave-function amplitude. Right: The amplitude of the final state at time $t = 250$ is represented on the A (red) and B (blue) sites of the lattice. **b.** The dynamical chiral polarization $\Pi_\psi(t) = \langle \Psi(t) | \mathcal{C}\hat{X} | \Psi(t) \rangle$ corresponding to the protocol described in **a** is constant in time (black solid line). By comparison, the dynamical chiral polarization starting from a state $\Psi_{AB}(t = 0)$ (resp. $\Psi_{BA}(t = 0)$), localized on two neighboring sites A and B (resp. B and A) shows fluctuations around the static chiral polarization whose amplitude depends on the initial state. The sign $\Pi_\psi(t)$ is reversed at short time when the chiral polarization of the initial state is opposite to the static chiral polarization of the SSH chain. This results in large amplitude oscillations. The short time dynamics of Π_ψ therefore provides a direct access to the orientation of the material chiral polarization.

455 We have shown that chiral symmetry alone translates real-space properties into spec-
 456 tral phases without relying on any crystalline symmetry and translational invariance when
 457 expressed as a sublattice symmetry. Chiral symmetry does not merely complement the
 458 classification of topological quantum chemistry [60–63] but also makes it possible to dis-
 459 tinguish topological phases in amorphous matter. In disordered system, introducing the
 460 concept of chiral polarization field, we provide a practical platform to detect topological
 461 phases coexisting in disordered samples, an to design robust zero-mode wave guides at
 462 their boundaries.

463 We expect our framework to extend beyond Hamiltonian dynamics when dissipative
 464 processes obey the chiral symmetry [64]. We therefore conjecture that real-space topol-
 465 ogy, geometry and non-Hermitian operator topology should cooperate in chiral dissipative
 466 materials as diverse as cold atoms to photonics, robotic devices and active matter.

467 Acknowledgements

468 We thank J. Asboth, A. Bernevig, A. Dauphin, K. Gawedzki, A. Grushin, Y. Hatsugai,
 469 P. Massignan, A. Po, A. Schnyder and A. Vishwanath for insightful discussions.

470 **Funding information** We acknowledge support from ANR WTF, and ToRe IdexLyon
 471 breakthrough programs.

472 A Bloch theory convention and Wannier states.

473 A.1 Conventions for the Bloch decomposition.

474 For the sake of clarity, we first introduce the main quantities used throughout all the
 475 manuscript to describe waves in periodic lattices. We note $|\Psi_{n,\mathbf{k}}\rangle$ the Bloch eigenstates.
 476 They correspond to wavefunctions $\langle \mathbf{x} | \Psi_{n,\mathbf{k}} \rangle = \varphi_{n,\mathbf{k}}(\mathbf{x}) e^{i\mathbf{k}\cdot\mathbf{x}}$, where \mathbf{k} is the momentum in
 477 the Brillouin Zone (BZ), and where the normalized function $\varphi_{n,\mathbf{k}}$ has a periodicity of one
 478 unit cell [28]. In this article, we use the following convention to express the Bloch states
 479 as a superposition of plane waves:

$$|\Psi_{n,\mathbf{k}}\rangle = \sum_{\alpha} u_{n,\alpha}(\mathbf{k}) |\mathbf{k}, \alpha\rangle, \quad (15)$$

480 where α labels the different atoms in the crystal, and $|\mathbf{k}, \alpha\rangle$ represents the Fourier trans-
 481 form of the real-space position basis: $|\mathbf{k}, \alpha\rangle = \sum_{\mathbf{R}} \exp(i\mathbf{k} \cdot \mathbf{R}) |\mathbf{R} + \mathbf{r}_{\alpha}\rangle$, \mathbf{R} being a Bravais
 482 lattice vector and \mathbf{r}_{α} a site position within the unit cell. We stress that here the compo-
 483 nents $u_{n,\alpha}(\mathbf{k})$ are periodic functions of \mathbf{k} over the BZ. It is worth noting, however, that
 484 there exists multiple conventions to decompose the Bloch states as discussed e.g in the
 485 context of graphene-like systems in [65–67]. A common alternative uses nonperiodic com-
 486 ponents over the BZ which carry an additional phase encoding the position of each atom
 487 within the unit cell: $|\Psi_{n,\mathbf{k}}\rangle = \sum_{\alpha} \tilde{u}_{n,\mathbf{k},\alpha} e^{i\mathbf{k}\cdot\mathbf{r}_{\alpha}} |\mathbf{k}, \alpha\rangle$. We will comment on the translation
 488 of our results from one convention to the other in the following.

489 A.2 Wannier functions.

490 By definition the Wannier function associated to a Bloch eigenstate is given by the inverse
491 Fourier transform (up to a phase):

$$|W_{n,\mathbf{R}}\rangle = \int_{\mathbf{k}} e^{-i\mathbf{k}\cdot\mathbf{R}} |\Psi_{n,\mathbf{k}}\rangle, \quad (16)$$

492 where $\int_{\mathbf{k}} \cdot \equiv \Omega^{-1} \int_{\text{BZ}} d^d k \cdot$, Ω being the volume of the BZ. Note that for sake of clarity, we
493 here and henceforth assume that the spectrum does not include band crossings. The tech-
494 nical generalization of our results to degenerated spectra is straightforward but involves
495 some rather heavy algebra, see e.g. [28].

497 A.3 Projected position operator and sublattice Zak phases.

498 Ignoring the distinction between the A and B sites, we can first compute the action of the
499 position operator on the Wannier states following [28]:

$$\begin{aligned} \langle \mathbf{x} | \hat{X} | W_{n,\mathbf{R}} \rangle &= \int_{\mathbf{k}} \mathbf{x} e^{i\mathbf{k}\cdot(\mathbf{x}-\mathbf{R})} \varphi_{n,\mathbf{k}}(\mathbf{x}) \\ &= \int_{\mathbf{k}} \left(-i\partial_{\mathbf{k}} e^{i\mathbf{k}\cdot(\mathbf{x}-\mathbf{R})} + \mathbf{R} e^{i\mathbf{k}\cdot(\mathbf{x}-\mathbf{R})} \right) \varphi_{n,\mathbf{k}}(\mathbf{x}) \\ &= \int_{\mathbf{k}} e^{-i\mathbf{k}\cdot\mathbf{R}} \left[e^{i\mathbf{k}\cdot\mathbf{x}} (\mathbf{R} + i\partial_{\mathbf{k}}) \right] \varphi_{n,\mathbf{k}}(\mathbf{x}), \end{aligned} \quad (17)$$

500 where in the last step we applied an integration by parts, using that $|\Psi_{n,\mathbf{k}}\rangle = |\Psi_{n,\mathbf{k}+\mathbf{G}}\rangle$ with
501 \mathbf{G} a primitive reciprocal vector. The generalization of Eq. (17) to the position operator
502 projected on the sublattice $a = A, B$ is straightforward:

$$\langle \mathbf{x} | \hat{X} \mathbb{P}^a | W_{n,\mathbf{R}} \rangle = \int_{\mathbf{k}} e^{-i\mathbf{k}\cdot\mathbf{R}} \left[e^{i\mathbf{k}\cdot\mathbf{x}} (\mathbf{R} + i\partial_{\mathbf{k}}) \right] \mathbb{P}^a \varphi_{n,\mathbf{k}}(\mathbf{x}), \quad (18)$$

503 which allows us to define the average positions $\langle \mathbf{x}^a \rangle_{n,\mathbf{R}}$ restricted to the site $a = A, B$ and
504 to the n^{th} band excitations:

$$\begin{aligned} \langle \mathbf{x}^a \rangle_{n,\mathbf{R}} &\equiv \langle W_{n,\mathbf{R}} | \mathbb{P}^a \hat{X} \mathbb{P}^a | W_{n,\mathbf{R}} \rangle \\ &= \mathbf{R} \int_{\mathbf{k}} \langle \varphi_{n,\mathbf{k}} | \mathbb{P}^a | \varphi_{n,\mathbf{k}} \rangle + \frac{1}{\Omega} \mathbf{\Gamma}_{\text{Zak}}^a(n), \end{aligned} \quad (19)$$

505 where Ω is the volume of the BZ, $|\varphi_{n,\mathbf{k}}\rangle = e^{-i\mathbf{k}\cdot\hat{X}} |\Psi_{n,\mathbf{k}}\rangle$, and $\mathbf{\Gamma}_{\text{Zak}}^a(n)$ is the vector com-
506 posed of the d sublattice Zak phases associated to the n -th band:

$$\mathbf{\Gamma}_{\text{Zak}}^a(n) = i\Omega \int_{\mathbf{k}} \langle \varphi_{n,\mathbf{k}} | \mathbb{P}^a \partial_{\mathbf{k}} \mathbb{P}^a | \varphi_{n,\mathbf{k}} \rangle. \quad (20)$$

507 We can further simplify Eq. (19) noting that the orthonormality of the $|\varphi_{n,\mathbf{k}}\rangle$ implies
508 $\langle \varphi_{n,\mathbf{k}} | \mathbb{P}^A + \mathbb{P}^B | \varphi_{n,\mathbf{k}} \rangle = 1$ and $\langle \varphi_{n,\mathbf{k}} | \mathbb{P}^A - \mathbb{P}^B | \varphi_{n,\mathbf{k}} \rangle = 0$, which yields $\langle \varphi_{n,\mathbf{k}} | \mathbb{P}^a | \varphi_{n,\mathbf{k}} \rangle =$
509 $1/2$. All in all, we find a simple relation between the average of the position operator and
510 the Zak phase of the Bloch eigenstates over the BZ:

$$\langle \mathbf{x}^a \rangle_{n,\mathbf{R}} = \frac{\mathbf{R}}{2} + \frac{1}{\Omega} \mathbf{\Gamma}_{\text{Zak}}^a(n). \quad (21)$$

511 B Chiral polarization, Zak phases and winding.

512 B.1 Chiral polarization and sublattice Zak phases.

513 We are now equipped to compute the chiral polarization, defined as the difference between
 514 the expected value of the projected position operators over the occupied eigenstates ($n <$
 515 0). It readily follows from Eq. (21) that $\mathbf{\Pi}$ corresponds to the difference of the sublattice
 516 Zak phases:

$$\begin{aligned} \mathbf{\Pi} &\equiv 2 \sum_{n < 0} \langle \mathbf{x}^A \rangle_{n, \mathbf{R}} - \langle \mathbf{x}^B \rangle_{n, \mathbf{R}} \\ &= \frac{2}{\Omega} \sum_{n < 0} \mathbf{\Gamma}_{\text{Zak}}^A(n) - \mathbf{\Gamma}_{\text{Zak}}^B(n). \end{aligned} \quad (22)$$

517 Two comments are in order. Firstly, the sum could have been also taken over the unoc-
 518 cupied states ($n > 0$). As $\mathbb{C}^2 = \mathbb{I}$, the sublattice phase picked up by $|\varphi_{n, \mathbf{k}}\rangle$ is indeed the
 519 same as that of its chiral partner $|\varphi_{-n, \mathbf{k}}\rangle = \mathbb{C} |\varphi_{n, \mathbf{k}}\rangle$. Secondly, we stress that Eq. (22)
 520 does not depend on the specific convention of the Bloch representation. This relation,
 521 however does not disentangle the respective contributions of the frame geometry and of
 522 the Hamiltonian on the chiral polarization. To single out the two contributions, we now
 523 use the specific Bloch representation (15). Given this choice, the sublattice Zak phase is
 524 naturally divided into two contributions leading to

$$\mathbf{\Gamma}_{\text{Zak}}^a(n) = \Omega \int_{\mathbf{k}} \sum_{\alpha \in a} (u_{n, \alpha}^* u_{n, \alpha} \mathbf{r}_\alpha + i u_{n, \alpha}^* \partial_{\mathbf{k}} u_{n, \alpha}). \quad (23)$$

525 The first term on the r.h.s. is the intracellular contribution to the Zak phase while the
 526 second is proportional to the sublattice intercellular Zak phase following to the definitions
 527 of [43]

$$\gamma_j^a(n) \equiv i \int dk_j \sum_{\alpha \in a} u_{n, \alpha}^*(\mathbf{k}) \partial_{k_j} u_{n, \alpha}(\mathbf{k}). \quad (24)$$

528 Summing Eq.(23) over all occupied bands, and using the orthogonality of the chiral com-
 529 ponent $u_{n, \alpha}$ we then recover our central result:

$$\mathbf{\Pi} = \mathbf{p} + \frac{2}{\Omega^{1/d}} (\gamma^A - \gamma^B), \quad (25)$$

530 where $\mathbf{p} = \sum_{\alpha \in A} \mathbf{r}_\alpha - \sum_{\alpha \in B} \mathbf{r}_\alpha$ is the geometrical polarization of the corresponding unit-
 531 cell and $\gamma^a = \sum_{n < 0} \gamma^a(n)$. The chiral polarization is the sum of one contribution coming
 532 only from the frame geometry and one contribution characterizing the geometrical phase
 533 of the Bloch eigenstates.

534

535 B.2 Chiral polarization in different Bloch conventions.

536 Although the physical content of the chiral polarization does not depend on the choice of
 537 the Bloch convention, it is worth explaining how to derive its functional form for the other
 538 usual representation where $|\Psi_{n, \mathbf{k}}\rangle = \sum_{\alpha} \tilde{u}_{n, \alpha}(\mathbf{k}) e^{i\mathbf{k} \cdot \mathbf{r}_\alpha} |\mathbf{k}, \alpha\rangle$. Within this convention the
 539 total Zak phase takes the form

$$\mathbf{\Gamma}_{\text{Zak}}^a(n) = i \int_{\text{BZ}} d^d k \sum_{\alpha \in a} \tilde{u}_{n, \alpha}^* \partial_{\mathbf{k}} \tilde{u}_{n, \alpha}, \quad (26)$$

540 which does not allow the distinction between the geometrical and the Hamiltonian con-
 541 tributions to Π when performing the sum over the occupied band in Eq. (22). This
 542 observation further justifies our choice for the Bloch representation.

543

544 B.3 Quantization of the intercellular Zak-phase in chiral insulators.

545 To demonstrate the quantization of $\gamma_j = \gamma_j^A + \gamma_j^B$, we resort to the Wilson loop formalism
 546 reviewed e.g. in Ref. [42].

547 Let us first recall the definition of the non-Abelian Berry-Wilczek-Zee connection along
 548 the Brillouin zone for a set of smooth vectors $|u_n(\mathbf{k})\rangle, n = 1, \dots, M$:

$$\mathbf{A}_{nm}(\mathbf{k}) = \langle u_n(\mathbf{k}) | \partial_{\mathbf{k}} | u_m(\mathbf{k}) \rangle. \quad (27)$$

549 The associated Wilson loop operator defined along the path \mathcal{C}_j through the Brillouin zone
 550 is given by the ordered exponential

$$W_j = \overline{\exp} \left(- \int_{\mathcal{C}_j} d\mathbf{k} \cdot \mathbf{A}(\mathbf{k}). \right) \quad (28)$$

551 The topological properties of a generic gapped chiral Hamiltonian are conveniently cap-
 552 tured by smooth deformations yielding a flat spectrum $E = \pm 1$. The corresponding Bloch
 553 Hamiltonian is then given by

$$H = \begin{pmatrix} 0 & Q(\mathbf{k}) \\ Q^\dagger(\mathbf{k}) & 0 \end{pmatrix} \quad (29)$$

554 where $Q(\mathbf{k})$ is a nonsingular unitary matrix. Without loss of generality, we write the
 555 corresponding eigenstates as

$$|u_{\pm n}(\mathbf{k})\rangle = \frac{1}{\sqrt{2}} \begin{pmatrix} \pm Q(\mathbf{k}) |e_n^B\rangle \\ |e_n^B\rangle \end{pmatrix} \quad (30)$$

556 where the sign \pm identifies the sign of the eigenvalue $E = \pm 1$ and the normalized vectors
 557 $|e_n^B\rangle$ form a basis of the Hilbert space of Q^\dagger . The non-Abelian connection (27) for the
 558 negative (resp. positive) energy states then takes the simple form

$$\mathbf{A}_{nm}^-(\mathbf{k}) = \frac{1}{2} \langle e_n^B | Q^\dagger(\mathbf{k}) \partial_{\mathbf{k}} Q(\mathbf{k}) | e_m^B \rangle = \mathbf{A}_{nm}^+(\mathbf{k}) \quad (31)$$

559 It follows from the definition of the Wilson-loop operator (Eq. (28)) that the intercellular
 560 Zak phase for the negative energy bands $\gamma = \gamma^A + \gamma^B$ is defined in terms of the Wilson
 561 loops for the non-Abelian connection $\mathbf{A}^-(\mathbf{k})$ as

$$\gamma_j = -i \ln \det W_j^- \quad (32)$$

562 The quantization of all d intercellular Zakk phases then follows from Eqs (28) and (31):

$$\gamma_j = -i \operatorname{tr} \ln \left[\overline{\exp} \left(-\frac{1}{2} \int_{\mathcal{C}_j} d\mathbf{k} \cdot \partial_{\mathbf{k}} \ln Q(\mathbf{k}) \right) \right] \quad (33)$$

$$= \pi w_j \operatorname{mod} (2\pi) \quad (34)$$

563 where the $\text{mod}(2\pi)$ indetermination stems from the choice of the branch cut of the
564 complex \ln function, and where w_j is the standard winding of the chiral Hamiltonian (29):

$$w_j = \frac{i}{4\pi} \int_{\mathcal{C}_j} d\mathbf{k} \cdot \text{tr} [\partial_{\mathbf{k}} H \mathbb{C} H^{-1}] \in \mathbb{Z}, \quad (35)$$

$$= \frac{1}{2\pi i} \int_{\mathcal{C}_j} d\mathbf{k} \cdot \text{tr} [Q^{-1} \partial_{\mathbf{k}} Q]. \quad (36)$$

565 We therefore conclude that the d Zak phases are topological phases defined modulo 2π .

566

567 **B.4 Relating the sublattice Zak phases to the winding of the Bloch** 568 **Hamiltonian.**

569 We here demonstrate the essential relation given by Eq. (9). To do so, we relate the
570 winding w_j to the sublattice Zak phases by evaluating the trace in Eq. (35) using the
571 eigenstate basis. Noting that $\langle u_n | \partial_{\mathbf{k}} H(\mathbf{k}) \mathbb{C} H^{-1}(\mathbf{k}) | u_n \rangle = -2 \langle u_n | \mathbb{C} \partial_{\mathbf{k}} | u_n \rangle$, the winding
572 takes the simple form

$$w_j = -\frac{i}{2\pi} \int_{\mathcal{C}_j} dk \sum_n \langle u_n | \mathbb{C} \partial_{\mathbf{k}} | u_n \rangle. \quad (37)$$

573 Decomposing the chiral operator on the two sublattice projectors $\mathbb{C} = \mathbb{P}^A - \mathbb{P}^B$, yields

$$\pi w_j = (\gamma_j^B - \gamma_j^A) \in \pi \mathbb{Z}. \quad (38)$$

574 **B.5 Quantization of the sublattice Zak phases.**

575 Eqs. (34) and (38) shows that both the sum and the difference of the sublattice Zak
576 phases are quantized:

$$\begin{aligned} \gamma_j^A + \gamma_j^B &= \pi w_j + 2\pi m, & m \in \pi \mathbb{Z}, \\ \gamma_j^B - \gamma_j^A &= \pi w_j. \end{aligned} \quad (39)$$

577 It then follows that both sublattice phases γ_j^A and γ_j^B are integer multiples of π .

578

579 **B.6 How does the winding number of a chiral Bloch Hamiltonian change** 580 **upon unit cell redefinition?**

581 Starting from a chiral Hamiltonian \mathcal{H} , we demonstrate below the relation between the
582 winding numbers associated to the Bloch Hamiltonians constructed from different choices
583 of unit cells, Eq. (11).

584 The definition of Bloch waves and Bloch Hamiltonians require prescribing a unit cell.
585 Starting with a first choice of a unit cell geometry, say unit cell (1), we can write $H^{(1)}(\mathbf{k})$
586 in the chiral basis as

$$H^{(1)}(\mathbf{k}) = \begin{pmatrix} 0 & Q^{(1)} \\ Q^{\dagger(1)} & 0 \end{pmatrix}, \quad (40)$$

587 Let us now opt for a second choice of unit cell, say choice (2). The Bloch Hamiltonians
588 $H^{(1)}$ and $H^{(2)}$ are then related by a unitary transformation

$$H^{(2)} = U^\dagger H^{(1)} U, \quad (41)$$

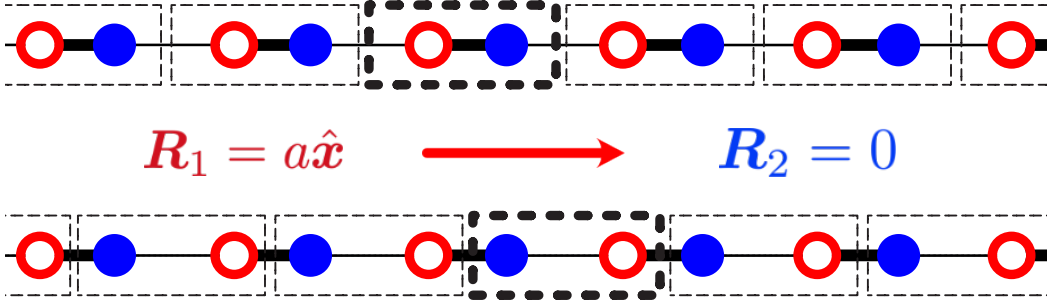


Figure 10: **Unit cell transformation.** We illustrate the definition of the \mathbf{R}_α vectors using the simple example of a SSH chain. For the first atom (empty symbol) $\mathbf{R}_1 = a\hat{x}$ while $\mathbf{R}_2 = 0$ for the second atom (solid symbol).

589 where the components of the unitary matrix are given by

$$U_{\alpha\beta} = \exp\left(i\mathbf{k} \cdot \mathbf{R}_\alpha^{(12)}\right) \delta_{\alpha\beta}, \quad (42)$$

590 where the \mathbf{R}_α^{12} are the Bravais vectors connecting the position of the atoms in the two unit-
 591 cell conventions, see Fig. 10 for a simple illustration. We note that, we have implicitly
 592 ignored the trivial redefinitions of the unit cell that reduce to permutations of the site
 593 indices. We can then express the winding of $H^{(2)}$ using Eq. (41) in the definition of
 594 Eq. (35), which yields

$$w_j^{(2)} = \frac{i}{4\pi} \int_{\mathcal{C}_j} d\mathbf{k} \operatorname{tr} \left[\partial_{\mathbf{k}} (UH^{(1)}U^\dagger) \mathcal{C} (UH^{(1)}U^\dagger)^{-1} \right]. \quad (43)$$

595 Expanding the gradient, using the trace cyclic property and noting that $[\mathcal{C}, U] = 0$, we
 596 find

$$w_j^{(2)} = w_j^{(1)} - \frac{i}{2\pi} \int_{\mathcal{C}_j} d\mathbf{k} \operatorname{tr} [\partial_{\mathbf{k}} U \mathcal{C} U^{-1}]. \quad (44)$$

597 This equation relates the winding numbers of the two Bloch Hamiltonians to the winding
 598 number of the transformation matrix U , which is by definition a geometrical quantity
 599 independent of \mathcal{H} . Using Eq. (42) leads to the remarkable relation which relates the
 600 spectral properties of the Hamiltonian to the unit-cell geometry

$$w_j^{(1)} - w_j^{(2)} = \frac{i}{2\pi} \int_{\mathcal{C}_j} d\mathbf{k} \operatorname{tr} [\partial_{\mathbf{k}} U \mathcal{C} U^{-1}] = \frac{1}{a_j} \left(\sum_{\alpha \in A} R_\alpha - \sum_{\alpha \in B} R_\alpha \right). \quad (45)$$

601 C Zero energy flat-band insulators.

602 We consider a flat-band chiral insulator, defined on a lattice with an non-vanishing chiral
 603 charge. In mechanics this situation is readily achieved adding extra bonds to further
 604 rigidify an otherwise isostatic lattice. It is characterized by a finite gap separating positive

605 and negative energy states and by an additional flat band at $E = 0$. In such a phase, there
 606 may exist additional zero energy edge states in addition to the bulk zero-energy modes.
 607 These edge states are analogous to the topological edge modes of insulators. Our goal is
 608 here to derive a bulk-boundary correspondence for these materials and provide a count of
 609 their zero-energy edge states. We will show that this correspondence involves the specific
 610 geometry of the eigenstates as opposed to their topology in the case of genuine insulators.

611 To show this we first derive the expression of the chiral polarization in the presence
 612 of a finite bulk chiral charge. Our starting point is Eq. (22), which relates to the chiral
 613 polarization of a crystal to the sublattice Zak phases given by Eq. (20):

$$\mathbf{\Pi} \equiv 2 \sum_{n < 0} \langle \mathbf{x}^A \rangle_{n, \mathbf{R}} - \langle \mathbf{x}^B \rangle_{n, \mathbf{R}} = \frac{2}{\Omega} \sum_{n < 0} \mathbf{\Gamma}_{\text{Zak}}^A(n) - \mathbf{\Gamma}_{\text{Zak}}^B(n). \quad (46)$$

614 The sum over all the negative energy bands $n < 0$ is half the sum over the non-zero energy
 615 states $n \neq 0$ given by

$$\begin{aligned} \sum_{n \neq 0} \mathbf{\Gamma}^a(n) &= \Omega \int_{\mathbf{k}} \sum_{\alpha \in a} \sum_n u_{n, \alpha}^* u_{n, \alpha} \mathbf{r}_\alpha + \frac{2}{\Omega^{1/d}} \gamma^a \\ &= \Omega \int_{\mathbf{k}} \sum_{\alpha \in a} \left(1 - \sum_{n_0} u_{n_0, \alpha}^* u_{n_0, \alpha} \right) \mathbf{r}_\alpha + \frac{2}{\Omega^{1/d}} \gamma^a. \end{aligned} \quad (47)$$

616 In the last line, we single out the role of the bulk zero-energy modes indexed by n_0 . Using
 617 the above expression to evaluate the r.h.s. of Eq. (46), we find an expression similar to
 618 Eq. (25) in the main text:

$$\mathbf{\Pi} = (\mathbf{p} - \mathbf{p}_{\text{ZM}}) + \frac{2}{\Omega^{1/d}} (\gamma^A - \gamma^B). \quad (48)$$

619 A first noticeable difference with Eq. (25) is a spectral correction to the geometrical polar-
 620 ization stemming from the localized zero-energy bulk modes. This zero-mode polarization
 621 is given by

$$\mathbf{p}_{\text{ZM}} = -\Omega \int_{\mathbf{k}} \sum_{n_0} \left(\sum_{\alpha \in A} - \sum_{\alpha \in B} \right) u_{n_0, \alpha}^* u_{n_0, \alpha} \mathbf{r}_\alpha. \quad (49)$$

622 Three comments are in order. Firstly, we stress that while the geometrical polarization \mathbf{p}
 623 depends on the choice of origin in the presence of an excess of chiral charge, the difference
 624 $\mathbf{p} - \mathbf{p}_{\text{ZM}}$, and $\mathbf{\Pi}$, are both independent of the frame's origin. Secondly, unlike in insulators,
 625 the difference between the intercellular sublattice Zak phases, $\gamma^A - \gamma^B$ does not identify
 626 with the winding number of the Bloch Hamiltonian. In fact it is not a topological quantity:
 627 it continuously depends on the specific couplings of the Hamiltonian. Finally, we point
 628 that, by definition, the chiral polarization does not depend on the Bloch convention.
 629 A change in the Bloch convention changes the geometrical polarization, the zero-mode
 630 polarization, and the intercellular zak phases in such a way that all corrections cancel one
 631 another.

632 Equipped with Eq. (48), we now turn to the generalization of the bulk boundary
 633 correspondence for flat-band insulators. We consider a crystalline material \mathcal{S} terminated
 634 by a clean edge $\partial\mathcal{S}$ oriented along the Bravais vector \mathbf{a}_1 . This edge may host \mathcal{V}^{NT} non-
 635 trivial zero-energy modes, in addition to the (trivial) bulk zero modes associated to the
 636 flat band. The edge defines a unit cell that may not be compatible with that of the
 637 atomic limit. We can nonetheless extend the edge region such that it matches the unit-cell
 638 compatible with the atomic limit (AL). The idea being that \mathcal{V}^{NT} is fully determined by
 639 the additional chiral charge of the edge with respect to that provided by the bulk chiral

640 charge density. Following the same reasoning as in the main text, this extra chiral charge
641 is given by the difference of geometrical polarization and zero-mode polarization:

$$\mathcal{V}^{\text{NT}} = \mathcal{N}^{\mathcal{B}} [(p_2 - p_{\text{ZM}_2})_{\text{AL}} - (p_2 - p_{\text{ZM}_2})], \quad (50)$$

642 where $\mathcal{N}^{\mathcal{B}}$ is the boundary length expressed in units of unit-cell length. The first term
643 is computed in the unit cell compatible with the atomic limit, and the second term is
644 computed in the original unit cell defined by the edge $\partial\mathcal{S}$.

645 The invariance of the chiral polarization with respect to unit cell transformations allows
646 the connection with the intercellular sublattice Zak phase:

$$\left(p_2 - p_{\text{ZM}_2} + \frac{2}{\Omega^{1/d}} (\gamma_2^A - \gamma_2^B) \right)_{\text{AL}} = p_2 - p_{\text{ZM}_2} + \frac{2}{\Omega^{1/d}} (\gamma_2^A - \gamma_2^B), \quad (51)$$

647 where AL denotes the terms evaluated in the unit-cell compatible with the atomic limit.
648 All in all, the non-trivial zero-energy content of flat band insulators is given by a formula
649 which generalizes Eq. (13):

$$\mathcal{V}^{\text{NT}} = \mathcal{N}^{\mathcal{B}} \frac{2}{\Omega^{1/d}} [(\gamma_2^A - \gamma_2^B) - (\gamma_2^A - \gamma_2^B)_{\text{AL}}]. \quad (52)$$

650 It is worth noting that in the case of genuine insulator, $(\gamma_2^A - \gamma_2^B)_{\text{AL}} = -w_{\text{AL}} = 0$ since it
651 corresponds to the winding number in the unit cell compatible with the AL. Once again
652 the chiral polarization field and its relation with the geometric phases allow us to predict
653 the existence of non-trivial zero-energy modes by observing the local discontinuities of the
654 chiral polarization field at any interface.

655 D Chiral polarization in amorphous materials.

656 We have seen that the chiral polarization does not depend on the specifics of the unit cell:
657 it is an intrinsic property of the material. In fact, as we show below, this framework is far
658 more general and we can define the chiral polarization in amorphous solids.

659 We start by revisiting the definition of the chiral polarization in a crystal given by
660 eq. (22):

$$\mathbf{\Pi} \equiv 2 \sum_{n < 0} \langle \mathbf{x}^A \rangle_{n, \mathbf{R}} - \langle \mathbf{x}^B \rangle_{n, \mathbf{R}}. \quad (53)$$

661 Strictly speaking this polarization is defined at the position \mathbf{R} . However, the discrete
662 translational invariance of the crystal and by consequence, of the Wannier functions, makes
663 the polarization field homogeneous. We can thus drop the \mathbf{R} indices.

664 The definition of the Wannier function as the inverse Fourier transform of the Bloch
665 eigenstate cannot be used when dealing with a disordered configuration. Instead, we work
666 with a another set of fully localized functions: the eigenstates of the projected position
667 operator onto the occupied bands [42]. The projected position operator is given by $P\hat{X}P$,
668 where

$$P = \sum_{E < 0} |\Psi_E(\mathbf{r})\rangle \langle \Psi_E(\mathbf{r})|, \quad (54)$$

669 is the projector onto the occupied energy states (not to be confused with the projectors
670 \mathbb{P}^a), and the $|\Psi_E\rangle$ are the eigenstates of the real space hamiltonian \mathcal{H} . Let us denote
671 the m^{th} eigenstate of the projected position operator as \widetilde{W}_m (notice that there are as

672 many eigenstates as occupied energy states of the Hamiltonian). This is a localized func-
 673 tion around the center given by $\mathbf{x}_m = \langle \widetilde{W}_m | \widehat{X} | \widetilde{W}_m \rangle$, similarly to the Wannier centers.
 674 Moreover, using each localized function, we can compute the difference of the weighted
 675 positions on both sublattices, in other words, the local chiral polarization:

$$\mathbf{\Pi}(\mathbf{x}_m) = 2 \langle \widetilde{W}_m | \mathbb{C}\widehat{X} | \widetilde{W}_m \rangle \quad (55)$$

676 In a periodic frame, the eigenstates of the projected position operator reduce to a linear
 677 combination of the Wannier functions W_n : $|\widetilde{W}_m\rangle = \sum_n V_{mn} |W_n\rangle$, with $n < 0$, indicating
 678 the occupied energy bands, V a unitary matrix in the energy space, and V_{mn} a diagonal
 679 matrix in the position space. We can then rewrite the chiral polarization in eq. (55) as

$$\begin{aligned} \mathbf{\Pi}(\mathbf{x}_m) &= 2 \sum_{n,l} \langle W_n | V_{mn}^\dagger \mathbb{C} V_{ml} | W_l \rangle \\ &= 2 \sum_{n < 0} \langle W_n | \mathbb{C}\widehat{X} | W_n \rangle, \end{aligned} \quad (56)$$

680 where in the last line we used the fact that the V_{ml} commutes with $\mathbb{C}\widehat{X}$ and the unitarity
 681 of V . As a result, we recover the first expression defined in crystals using the Bloch
 682 formalism as given by Eq. (22).

683 E Chiral polarization of time evolved Wannier states.

684 In Ref. [57], the mean chiral displacement under Hamiltonian dynamics was introduced as a
 685 measure of the Zak phase of periodic Hamiltonians in $d = 1$. This quantity characterizes a
 686 representation of a Hamiltonian associated to a given unit cell definition, and corresponds
 687 to the long-time displacement of an initially fully localized state, measured in units of
 688 the unit-cell size. As a consequence, several choices of unit cells were necessary to fully
 689 characterize the dynamics of a given (meta)material [56]. Although seemingly similar in
 690 its formal definition, the chiral polarization which we extensively use in this article is an
 691 intrinsic (meta)material property, defined in real space, and which does not rely on any
 692 underlying frame periodicity, Eq. (5). In the specific case of periodic frames $\mathbf{\Pi}$ crucially
 693 resolves the chiral imbalance of wave packets with a sub-unit-cell resolution.

694 In this method section, we show how $\mathbf{\Pi}$ relates to the dynamics of a maximally localized
 695 Wannier state spreading in the bulk of a chiral crystal. To do so we consider the time
 696 evolution of a wave function $|\psi_n(t)\rangle = U(t) |W_{n,\mathbf{R}}\rangle$ starting from a of a Wannier state in
 697 band n , initially localized at \mathbf{R} , with an evolution operator $U(t) = \exp(-iHt)$. Using the
 698 notations introduced in Eq. (16), the position at time t is given by

$$\begin{aligned} \langle \mathbf{x} | \widehat{X} | \psi_n(t) \rangle &= \int_{\mathbf{k}} \mathbf{x} e^{i\mathbf{k}\cdot(\mathbf{x}-\mathbf{R})} e^{-iE_n(\mathbf{k})t} \varphi_{n,\mathbf{k}}(\mathbf{x}) \end{aligned} \quad (57)$$

$$= \int_{\mathbf{k}} e^{-i\mathbf{k}\cdot\mathbf{R}} \left[e^{i\mathbf{k}\cdot\mathbf{x}} (\mathbf{R} + \mathbf{v}_n(\mathbf{k})t + i\partial_{\mathbf{k}}) \right] \varphi_{n,\mathbf{k}}(\mathbf{x}), \quad (58)$$

699 where $\mathbf{v}_n(\mathbf{k}) = \partial_{\mathbf{k}} E_n(\mathbf{k})$ is the group velocity in the energy band n . We can also generalize
 700 Eq. (21) to define the instantaneous average positions restricted to the $a = A, B$ sublattices

701 which read

$$\langle \mathbf{x}^a(t) \rangle_{n,\mathbf{R}} \equiv \langle \psi_n(t) | \mathbb{P}^a \hat{X} \mathbb{P}^a | \psi_n(t) \rangle \quad (59)$$

$$= \oint_{\mathbf{k}} \frac{1}{2} (\mathbf{R} + \mathbf{v}_n(\mathbf{k})t) + \frac{1}{\Omega} \Gamma_{\text{Zak}}^a(n) \quad (60)$$

$$= \frac{1}{2} \mathbf{R} + \frac{1}{\Omega} \Gamma_{\text{Zak}}^a(n) \quad (61)$$

$$= \langle \mathbf{x}^a(t=0) \rangle_{n,\mathbf{R}}. \quad (62)$$

702 This result indicates that the chiral polarization of each Wannier state is a stationary
 703 quantity although they all evolve in time. When summed over (half of) the spectrum, we
 704 recover the static definition of the chiral polarization

$$\mathbf{\Pi}(t) = \text{Tr}(U^{-1}(t) \mathbb{C} \hat{X} U(t)) \quad (63)$$

$$= \sum_n \langle \psi_n(t) | \mathbb{C} \hat{X} | \psi_n(t) \rangle \quad (64)$$

$$= 2 \sum_{n<0} \langle \mathbf{x}^A(t) \rangle_{n,\mathbf{R}} - \langle \mathbf{x}^B(t) \rangle_{n,\mathbf{R}}$$

$$= \frac{2}{\Omega} \sum_{n<0} \Gamma_{\text{Zak}}^A(n) - \Gamma_{\text{Zak}}^B(n). \quad (65)$$

705 We note that the trace operation in Eq. (63) can be evaluated using any basis of the
 706 Hilbert space, such as the ensemble of states fully localized on the A and B sites.

707 References

- 708 [1] F. Bloch, *Über die quantenmechanik der elektronen in kristallgittern*, Zeitschrift für
 709 Physik **52**, 555 (1929).
- 710 [2] Q. X.L., H. T.L. and Z. S.C., *Topological field theory of time-reversal invariant*
 711 *insulators*, Phys.Rev.B **78**(195424) (2008).
- 712 [3] M. Z. Hasan and C. L. Kane, *Colloquium: Topological insulators*, Rev. Mod. Phys.
 713 **82**, 3045 (2010), doi:[10.1103/RevModPhys.82.3045](https://doi.org/10.1103/RevModPhys.82.3045).
- 714 [4] B.A.Bernevig and T.L.Hughes, *Topological insulators and topological superconductors*,
 715 Princeton University Press (2013).
- 716 [5] M. Franz and L. Molenkamp, eds., *Topological Insulators*, vol. 6 of *Contemporary*
 717 *Concepts of Condensed Matter Science*, Elsevier, (2013).
- 718 [6] J.K.Asboth, L.Oroszlany and A.Palyi, *A short course on topological insulators: Band-*
 719 *structure topology and edge states in one and two dimensions*, Lecture Notes in
 720 Physics **919** (2016).
- 721 [7] N. P. Armitage, E. J. Mele and A. Vishwanath, *Weyl and dirac semimet-*
 722 *als in three-dimensional solids*, Rev. Mod. Phys. **90**, 015001 (2018),
 723 doi:[10.1103/RevModPhys.90.015001](https://doi.org/10.1103/RevModPhys.90.015001).
- 724 [8] A. P. Schnyder, S. Ryu, A. Furusaki and A. W. Ludwig, *Classification of topological*
 725 *insulators and superconductors in three spatial dimensions*, Physical Review B **78**(19),
 726 195125 (2008).

- 727 [9] A. Kitaev, *Periodic table for topological insulators and superconductors*, In *AIP*
728 *Conference Proceedings*, vol. 1134, pp. 22–30. AIP (2009).
- 729 [10] S. Ryu, A. P. Schnyder, A. Furusaki and A. W. W. Ludwig, *Topological insulators*
730 *and superconductors: tenfold way and dimensional hierarchy*, *New Journal of Physics*
731 **12**(6), 065010 (2010).
- 732 [11] L. Fidkowski, T. S. Jackson and I. Klich, *Model characterization of gapless edge modes*
733 *of topological insulators using intermediate brillouin-zone functions*, *Phys. Rev. Lett.*
734 **107**, 036601 (2011), doi:[10.1103/PhysRevLett.107.036601](https://doi.org/10.1103/PhysRevLett.107.036601).
- 735 [12] A. Alexandradinata, X. Dai and B. A. Bernevig, *Wilson-loop characterization of*
736 *inversion-symmetric topological insulators*, *Phys. Rev. B* **89**, 155114 (2014).
- 737 [13] M. Taherinejad, K. F. Garrity and D. Vanderbilt, *Wannier center sheets in topological*
738 *insulators*, *Phys. Rev. B* **89**, 115102 (2014).
- 739 [14] A. Alexandradinata, Z. Wang and B. A. Bernevig, *Topological insulators from group*
740 *cohomology*, *Phys. Rev. X* **6**, 021008 (2016).
- 741 [15] A. Alexandradinata and B. A. Bernevig, *Berry-phase description of topological crys-*
742 *talline insulators*, *Phys. Rev. B* **93**, 205104 (2016).
- 743 [16] R. Jackiw and C. Rebbi, *Solitons with fermion number 1/2*, *Physical Review D*
744 **13**(12), 3398 (1976).
- 745 [17] B. Volkov and O. Pankratov, *Two-dimensional massless electrons in an inverted*
746 *contact*, *Soviet Journal of Experimental and Theoretical Physics Letters* **42**, 178
747 (1985).
- 748 [18] E. Fradkin, E. Dagotto and D. Boyanovsky, *Physical realization of the parity anomaly*
749 *in condensed matter physics*, *Physical review letters* **57**(23), 2967 (1986).
- 750 [19] Y. Hatsugai, *Chern number and edge states in the integer quantum hall effect*, *Phys.*
751 *Rev. Lett.* **71**, 3697 (1993), doi:[10.1103/PhysRevLett.71.3697](https://doi.org/10.1103/PhysRevLett.71.3697).
- 752 [20] T. Ozawa, H. M. Price, A. Amo, N. Goldman, M. Hafezi, L. Lu, M. C. Rechtsman,
753 D. Schuster, J. Simon, O. Zilberberg and I. Carusotto, *Topological photonics*, *Rev.*
754 *Mod. Phys.* **91**, 015006 (2019), doi:[10.1103/RevModPhys.91.015006](https://doi.org/10.1103/RevModPhys.91.015006).
- 755 [21] X. Mao and T. C. Lubensky, *Maxwell lattices and topological mechanics*, *Annual*
756 *Review of Condensed Matter Physics* **9**, 413 (2018).
- 757 [22] A. J. Heeger, S. Kivelson, J. R. Schrieffer and W. P. Su, *Solitons in conducting*
758 *polymers*, *Rev. Mod. Phys.* **60**, 781 (1988), doi:[10.1103/RevModPhys.60.781](https://doi.org/10.1103/RevModPhys.60.781).
- 759 [23] V. Gurarie and J. T. Chalker, *Some generic aspects of bosonic excitations in disor-*
760 *dered systems*, *Phys. Rev. Lett.* **89**, 136801 (2002).
- 761 [24] V. Gurarie and J. T. Chalker, *Bosonic excitations in random media*, *Phys. Rev. B*
762 **68**, 134207 (2003).
- 763 [25] C. Kane and T. Lubensky, *Topological boundary modes in isostatic lattices*, *Nature*
764 *Physics* **10**(1), 39 (2014).
- 765 [26] S. D. Huber, *Topological mechanics*, *Nature Physics* **12**(7), 621 (2016).

- 766 [27] J. Zak, *Berry's phase for energy bands in solids*, Phys. Rev. Lett. **62**, 2747 (1989).
- 767 [28] D. Vanderbilt, *Berry Phases in Electronic Structure Theory*, Cambridge University
768 Press (2018).
- 769 [29] D. Vanderbilt and R. D. King-Smith, *Electric polarization as a bulk quantity and its
770 relation to surface charge*, Phys. Rev. B **48**, 4442 (1993).
- 771 [30] R. D. King-Smith and D. Vanderbilt, *Theory of polarization of crystalline solids*,
772 Phys. Rev. B **47**, 1651(R) (1993).
- 773 [31] L. Fu and C. Kane, *Time reversal polarization and a z_2 adiabatic spin pump*, Phys.
774 Rev. B **74**, 195312 (2006).
- 775 [32] T. Louvet, P. Delplace, A. A. Fedorenko and D. Carpentier, *Minimal conductivity,
776 topological berry winding and duality in three-band semimetals*, Phys. Rev. B **92**,
777 155116 (2015).
- 778 [33] J. C. Maxwell, *On the calculation of the equilibrium and stiffness of frames*, The Lon-
779 don, Edinburgh, and Dublin Philosophical Magazine and Journal of Science **27**(182),
780 294 (1864).
- 781 [34] C. Calladine, *Buckminster fuller's "tensegrity" structures and clerk maxwell's rules
782 for the construction of stiff frames*, International journal of solids and structures
783 **14**(2), 161 (1978).
- 784 [35] B. Sutherland, *Localization of electronic wave functions due to local topology*, Phys.
785 Rev. B **34**, 5208 (1986).
- 786 [36] I. Mondragon-Shem, T. L. Hughes, J. Song and E. Prodan, *Topological criticality
787 in the chiral-symmetric aiii class at strong disorder*, Phys. Rev. Lett. **113**, 046802
788 (2014), doi:[10.1103/PhysRevLett.113.046802](https://doi.org/10.1103/PhysRevLett.113.046802).
- 789 [37] T. Rakovszky, J. K. Asbóth and A. Alberti, *Detecting topological invariants
790 in chiral symmetric insulators via losses*, Phys. Rev. B **95**, 201407 (2017),
791 doi:[10.1103/PhysRevB.95.201407](https://doi.org/10.1103/PhysRevB.95.201407).
- 792 [38] F. Cardano, A. D'Errico, A. Dauphin, M. Maffei, B. Piccirillo, C. de Lisio, G. De Fil-
793 ippis, V. Cataudella, E. Santamato, L. Marrucci *et al.*, *Detection of zak phases and
794 topological invariants in a chiral quantum walk of twisted photons*, Nature communi-
795 cations **8**(1), 1 (2017).
- 796 [39] D. Z. Rocklin, *Directional mechanical response in the bulk of topological metamateri-
797 als*, New Journal of Physics **19**(6), 065004 (2017).
- 798 [40] O. R. Bilal, R. Süsstrunk, C. Daraio and S. D. Huber, *Intrinsically polar elastic
799 metamaterials*, Advanced Materials **29**(26), 1700540 (2017).
- 800 [41] E. Blount, *Formalisms of band theory*, In *Solid state physics*, vol. 13, pp. 305–373.
801 Elsevier (1962).
- 802 [42] T. Neupert and F. Schindler, *Topological crystalline insulators*, In *Topological Matter*,
803 pp. 31–61. Springer (2018).
- 804 [43] J.-W. Rhim, J. Behrends and J. H. Bardarson, *Bulk-boundary correspondence from
805 the intercellular zak phase*, Phys. Rev. B **95**, 035421 (2017).

- 806 [44] For illustrative purposes we used a gauge transformation $e^{i\alpha(k)}$, $\alpha(ka) = 0.3 \cos(ka)$
807 to best demonstrate the asymmetric spreading of the localized states.
- 808 [45] J. Jiang and S. G. Louie, *Topology classification using chiral symmetry and spin*
809 *correlations in graphene nanoribbons*, Nano Letters (2020).
- 810 [46] X. Zhang, M. Xiao, Y. Cheng, M.-H. Lu and J. Christensen, *Topological sound*,
811 *Communications Physics* **1**(1), 1 (2018).
- 812 [47] N. P. Mitchell, L. M. Nash, D. Hexner, A. M. Turner and W. T. Irvine, *Amorphous*
813 *topological insulators constructed from random point sets*, *Nature Physics* **14**(4), 380
814 (2018).
- 815 [48] M. Xiao and S. Fan, *Photonic chern insulator through homogenization of an array of*
816 *particles*, *Phys. Rev. B* **96**, 100202 (2017), doi:[10.1103/PhysRevB.96.100202](https://doi.org/10.1103/PhysRevB.96.100202).
- 817 [49] A. Agarwala and V. B. Shenoy, *Topological insulators in amorphous systems*, *Phys.*
818 *Rev. Lett.* **118**, 236402 (2017), doi:[10.1103/PhysRevLett.118.236402](https://doi.org/10.1103/PhysRevLett.118.236402).
- 819 [50] Q. Marsal, D. Varjas and A. G. Grushin, *Topological weaire-thorpe models of amor-*
820 *phous matter*, arXiv preprint arXiv:2003.13701 (2020).
- 821 [51] G. H. Golub and C. F. Van Loan, *Matrix computations*, vol. 3, JHU press (2013).
- 822 [52] E. J. Meier, F. A. An, A. Dauphin, M. Maffei, P. Massignan, T. L. Hughes and
823 B. Gadway, *Observation of the topological anderson insulator in disordered atomic*
824 *wires*, *Science* **362**(6417), 929 (2018).
- 825 [53] M. Bellec, U. Kuhl, G. Montambaux and F. Mortessagne, *Topological transition*
826 *of dirac points in a microwave experiment*, *Phys. Rev. Lett.* **110**, 033902 (2013),
827 doi:[10.1103/PhysRevLett.110.033902](https://doi.org/10.1103/PhysRevLett.110.033902).
- 828 [54] A. Agarwala, V. Juričić and B. Roy, *Higher-order topological insu-*
829 *lators in amorphous solids*, *Phys. Rev. Research* **2**, 012067 (2020),
830 doi:[10.1103/PhysRevResearch.2.012067](https://doi.org/10.1103/PhysRevResearch.2.012067).
- 831 [55] M. Serra-Garcia, V. Peri, R. Süsstrunk, O. R. Bilal, T. Larsen, L. G. Villanueva and
832 S. D. Huber, *Observation of a phononic quadrupole topological insulator*, *Nature*
833 **555**(7696), 342 (2018).
- 834 [56] F. Cardano, A. D’Errico, A. Dauphin, M. Maffei, B. Piccirillo, C. de Lisio, G. De Fil-
835 ippis, V. Cataudella, E. Santamato, L. Marrucci *et al.*, *Detection of Zak phases and*
836 *topological invariants in a chiral quantum walk of twisted photons*, *Nature communi-*
837 *cations* **8**(1), 1 (2017).
- 838 [57] M. Maffei, A. Dauphin, F. Cardano, M. Lewenstein and P. Massignan, *Topological*
839 *characterization of chiral models through their long time dynamics*, *New Journal of*
840 *Physics* **20**(1), 013023 (2018).
- 841 [58] P. St-Jean, A. Dauphin, P. Massignan, B. Real, O. Jamadi, M. Milićević, A. Lemaître,
842 A. Harouri, L. L. Gratiet, I. Sagnes *et al.*, *Measuring topological invariants in polari-*
843 *tonic graphene*, arXiv preprint arXiv:2002.09528 (2020).
- 844 [59] A. D’Errico, F. Di Colandrea, R. Barboza, A. Dauphin, M. Lewenstein, P. Massignan,
845 L. Marrucci and F. Cardano, *Bulk detection of time-dependent topological transitions*
846 *in quenched chiral models*, *Physical Review Research* **2**(2), 023119 (2020).

- 847 [60] J. Kruthoff, J. de Boer, J. van Wezel, C. L. Kane and R.-J. Slager, *Topological*
848 *classification of crystalline insulators through band structure combinatorics*, Phys.
849 Rev. X **7**, 041069 (2017), doi:[10.1103/PhysRevX.7.041069](https://doi.org/10.1103/PhysRevX.7.041069).
- 850 [61] B. Bradlyn, L. Elcoro, J. Cano, M. Vergniory, Z. Wang, C. Felser, M. Aroyo and
851 B. A. Bernevig, *Topological quantum chemistry*, Nature **547**(7663), 298 (2017).
- 852 [62] F. Tang, H. C. Po, A. Vishwanath and X. Wan, *Comprehensive search for topological*
853 *materials using symmetry indicators*, Nature **566**(7745), 486 (2019).
- 854 [63] T. Zhang, Y. Jiang, Z. Song, H. Huang, Y. He, Z. Fang, H. Weng and C. Fang,
855 *Catalogue of topological electronic materials*, Nature **566**(7745), 475 (2019).
- 856 [64] K. Kawabata, K. Shiozaki, M. Ueda and M. Sato, *Symmetry and topology in non-*
857 *hermitian physics*, Phys. Rev. X **9**, 041015 (2019), doi:[10.1103/PhysRevX.9.041015](https://doi.org/10.1103/PhysRevX.9.041015).
- 858 [65] C. Bena and G. Montambaux, *Remarks on the tight-binding model of graphene*, New
859 Journal of Physics **11**(9), 095003 (2009).
- 860 [66] J. Fuchs, F. Piéchon, M. Goerbig and G. Montambaux, *Topological berry phase and*
861 *semiclassical quantization of cyclotron orbits for two dimensional electrons in coupled*
862 *band models*, The European Physical Journal B **77**(3), 351 (2010).
- 863 [67] M. Fruchart, D. Carpentier and K. Gawedzki, *Parallel transport and band theory in*
864 *crystals*, EPL (Europhysics Letters) **106**(6), 60002 (2014).